

PAPER

Theoretical studies on the elastic scattering of e^{\pm} off the ions of xenon isonuclear series

To cite this article: Mahmudul H Khandker *et al* 2021 *Phys. Scr.* **96** 025402

View the [article online](#) for updates and enhancements.

You may also like

- [Dynamic charge state distributions of 5 MeV \$Xe^{20+}\$ ions penetrating through gaseous argon target](#)
Z Wang, R Cheng, F B Xue et al.
- [Guided transmission of xenon ions through single nanohole in PC foil](#)
Y Y Wang, Y T Zhao, G Xiao et al.
- [Modeling of a DC glow discharge in a neon–xenon gas mixture at low pressure and with metastable atom densities](#)
A BOUCHIKHI



PAPER

Theoretical studies on the elastic scattering of e^+ off the ions of xenon isonuclear seriesMahmudul H Khandker¹ , M Masum Billah¹ , Hiroshi Watabe² , A K F Haque^{1,3,4,*} and M Alfaz Uddin⁵ ¹ Atomic and Molecular Physics Lab, Department of Physics, University of Rajshahi. Rajshahi-6205, Bangladesh² Division of Radiation Protection and Safety Control, Cyclotron and Radioisotope Center, Tohoku University, 6-3 Aoba, Aramaki, Aoba, Sendai 980-8578 Japan³ Nanosciences African network (NANOAFNET), Materials Research Group (MRG), iThemba LABS-National Research Foundation (NRF), 1 Old Faure Road, 7129, PO Box 722, Somerset West, Western Cape Province, South Africa⁴ UNESCO-UNISA Africa Chair in Nanosciences/Nanotechnology Laboratories, College of Graduate Studies, University of South Africa (UNISA), Muckleneuk Ridge, PO Box 392, Pretoria, South Africa⁵ Department of Physics, Pabna University of Science and Technology. Pabna-6600, Bangladesh

* Author to whom any correspondence should be addressed.

E-mail: fhaque@ru.ac.bd**Keywords:** electron and positron-ion scattering, Coulomb glory, xenon ions, modified Coulomb field, isonuclear series**Abstract**

This work presents the calculations of differential, integrated elastic and momentum transfer cross sections for the elastic scattering of electrons from the ions of xenon isonuclear series over the incident energy range 1 eV–1000 eV. Coulomb glory, the amplification of elastic backscattering of electrons from positive ions owing to the electrostatic screening of nuclear potential by atomic electrons, is investigated throughout the ionic series of xenon, argon and neon. Cross sections for the angular distribution of elastically scattered positron from selected xenon ions are also calculated. Energy dependency of differential cross sections and Sherman functions are predicted for both the projectiles and a comparison is presented to exhibit the dissimilarity arising out of the difference of the interactions of the projectiles with ions. The theoretical methodology of this work employs the Dirac relativistic partial wave analysis using a complex optical potential, comprising static, exchange, polarization and imaginary components, and a pure Coulomb potential. The results obtained show reasonable agreements with the available experimental data and other theoretical calculations.

1. Introduction

Theory of the elastic scattering of electrons and positrons from positive ions provides some simple testing grounds of atomic structure and collision dynamics. Moreover this theory carries enormous importance for the spectroscopic clarifications and theoretical modeling of the formation and time evolution of artificial, terrestrial, space and astrophysical plasmas [1]. Data of electron-ion collisions are required in such applied and research areas as atmospheric physics, radiation dosimetry, nuclear medicine, radiation biology, radiotherapy, fusion energy research, semiconductor lithography, x-ray lasers, etc [2–4]. On the other side, interpreting the scattering of positron by positive ions opens the door to the new physics and applications complementary to the dynamics of electron-ion collisions. This antimatter and matter interaction provides a key to understand the propagation mechanisms of positrons in the interstellar medium through its collisions with the ionic gas of this medium and possibly place constraints on the origin of antimatter [5]. The use of xenon ions in medical implant [6], ion thruster [7], ion propulsion technology [6] and ion bombardment [8] makes this study interesting and useful.

Despite such importance from both theoretical and practical standpoints, works on electron-ion scattering, particularly across the isonuclear series, are limited in the literature. Measurements of electron-ion and positron-ion scattering observables are scarce due to the inherent low luminosity collisions of standard cross-beam experiments. Recent availability of multiply charged ion sources and advancement of technology provide the opportunity to

measure differential cross sections of these scattering. McKenna and Williams [9] measured the angular distribution of electrons scattered elastically from Xe^{2+} at 16 eV using a crossed-beam energy-loss spectrometer. Bélenger *et al* [10] published the experimental differential cross section data and Hatree-Fock calculations for the elastic scattering of electrons from Xe^{3+} at 43.07 eV, Xe^{4+} and Xe^{5+} at 43.83 eV at scattering angles between 32° and 148° . Huber *et al* [11] measured DCS for the elastic collisions of electrons by a well-focused beam of multiply charged xenon ions (Xe^{6+} and Xe^{8+}) at 50 eV delivered by an electron cyclotron resonance ion source and compared the data with their Hatree-Fock calculations. Also the measured data on the observable quantities of positron-ion scattering are very rare in literature owing to the complications in executing an experiment on this scattering system.

The aforesaid importance of collision data for e^\pm -ion scattering in various applied areas and the scope of understanding projectile-ion interaction, using these experimental data, have spurred the theoretical study of the elastic scattering of e^\pm from the ions of xenon isonuclear series. This study is also motivated to glean information on the charge (ionic) and energy dependence of the of various scattering observables. Previously we studied the features of isonuclear series of light and medium atoms, like nitrogen [3], neon [12] and argon [2]. Therefore it is an additional impetus to investigate how the above features across an isonuclear series emerges out for a heavy atom and to see whether a new physics content unfolds.

Theoretical study of e^\pm -ion scattering phenomenon entails a combination of a short-range and a long range potentials. The latter, largely responsible for the small angle collisions ($\theta \lesssim 50^\circ$), arises due to the interaction of the projectiles, e^\pm with the ionic charge of the target and is therefore dominated by long range Coulomb potential [13]. These distant collisions are well described by Rutherford scattering. On the other hand, short-range potential produces mostly the large angle collisions ($\theta \gtrsim 50^\circ$). This potential is the interaction of primary e^\pm with the bound electrons and a nuclear protons. These collisions are related to the small impact parameter or lower value of orbital angular momentum and are therefore a sensitive probe of atomic structure [13]. An interference structure in differential cross section (DCS) is observed in this high angular region.

Oscillations in the observed interference structures in DCS tend to show a maximum at a scattering angle of $\theta = 180^\circ$. This interesting phenomenon, termed as Coulomb glory, is observed in the scattering of electrons, mu-mesons and anti-protons by multiply charged ions [10, 14]. This feature is contrary to the pure Coulomb scattering, in which cross section for the collision at an angle $\theta \sim 180^\circ$ is always observed to show a smooth minimum with the increase of orbital angular momentum or impact parameter [15]. A potential with attractive Coulomb core possesses a power singularity ($U(r) \approx -Z/r$), hence the projectile electron does not have any choice other than getting scattered through $\theta = 180^\circ$ for vanishingly small orbital angular momentum. This feature, known as rainbow effect, is intrinsic for potential with an attractive Coulomb core [16]. When the naked nucleus is dressed by an electron cloud, nuclear potential observes an electrostatic screening by these atomic electrons that slows down the aforesaid decrease of scattering angle at which the maximum in DCS occurs. When the energy is low enough relative to the potential of the electrostatic screening at the nucleus, the scattering angle increases instead of decrease and the scattered electron faces backward glory for non-zero orbital angular momentum [14, 15]. Combination of these low energy and screening effects, termed as Coulomb glory, amplifies the DCS, for the scattering of electron by screened attractive Coulomb potential, in the angular zone $90^\circ < \theta < 180^\circ$ and a maximum is observed at $\theta = 180^\circ$ [14, 15]. Throughout the isonuclear series, when the number of dressing electrons of the target ion matches with the required low incident energy, the maximum at $\theta = 180^\circ$ exceeds the corresponding Rutherford DCS by several or several hundred times [17].

Asymptotic Coulomb potential is complemented by a short-range complex optical potential to explain this e^\pm -ion collision features. This combination of potentials, known as modified Coulomb potential, is used to calculate the observable quantities for e^\pm - Xe^{q+} elastic scattering by solving Dirac relativistic equation within the framework of partial wave analysis. The main reason for adopting the Dirac partial wave analysis in our investigation is that this relativistic approach automatically incorporates the spin-orbit term while Schrödinger equation requires the inclusion of this interaction term separately in the collision dynamics [18, 19].

Modified Coulomb potential is the key to elucidate the interference structure in the differential cross sections and understand the interactions of dressing electrons between themselves and with the incident electrons [20]. The short-range part of this potential is a complex local optical potential comprising both real and imaginary parts. The real part consists of static, exchange and correlation-polarization potentials. Within static-field approximation, static potential is generated from the electrostatic interactions of the projectile with the target electrons and protons, using the Dirac-Fock electron density, generated from relativistic Hartree-Fock wavefunctions by Desclaux [21] and Fermi nuclear charge distribution [22] respectively. The semi-classical approximate local exchange potential given by Furness and McCarthy [23] is used to handle the non-local rearrangement collisions between primary and bound electrons arising due to their indistinguishability. The distortion of the target charge distribution by a primary electron or positron is described by the correlation-polarization potential (CPP), a combination of long range Buckingham potential and a short-range correlation potential [24]. The loss of incident flux from elastic channel to inelastic channels above the inelastic threshold is accounted for by a semi-relativistic imaginary potential proposed by Salvat *et al* [25].

Calculations of DCS for electron and positron and integrated elastic cross section (IECS), momentum transfer cross section (MTCS) and Sherman function for electron scattered elastically from the ions of xenon isonuclear series, over the incident energy range 1–1000 eV are performed using Dirac's relativistic partial wave analysis employing the aforesaid modified Coulomb potential. DCS and Sherman function, as a function of projectile energy, are illustrated for both electron and positron and a comparison of similar observables is also presented. Coulomb glory, an interesting feature of electron-ion scattering, is presented for the xenon isonuclear series along with that for neon and argon isonuclear series. Our predictions are illustrated graphically along with the available experimental data [9–11] and other theoretical calculations [10, 11].

The organization of the paper is as follows. In section 2, the outline of the theory is discussed. In section 3, results of our theory and comparison with existing data and calculations are given. In section 4, we have drawn conclusion on our results. In this manuscript, equations are expressed in CGS Gaussian units unless otherwise specified, however, most of the calculations in the FORTRAN code [25] are performed in Hartree atomic units in which $\hbar = m_e = e = 1$.

2. Theory

2.1. Interaction potential

The modified Coulomb potential, a combination of asymptotic pure Coulomb potential and the complex short-range potential, is used to study the e^\pm -ion collision and is given as

$$V_{mC}(r) = zqe^2/r + V_{sr}(r). \quad (1)$$

Here, $z = -1$ for electron and $z = 1$ for positron. The first term on the right-hand side of (1) is the Coulomb potential due to the Coulomb interaction between primary electron or positron, with e as magnitude of the electron charge, and the target ion of charge qe . The short-range potential, $V_{sr}(r)$ is given by the complex optical potential

$$V_{sr}(r) = V_{st}(r) + V_{ex}(r) + V_{cp}(r) - iW_{abs}(r). \quad (2)$$

Here, $V_{st}(r)$, $V_{ex}(r)$, $V_{cp}(r)$ and $W_{abs}(r)$ are static, exchange, correlation-polarization and absorption potentials, respectively. For positron scattering, there is no exchange probability between the projectile and bound electrons, leading to $V_{ex}(r) = 0$.

Static potential arises from the electrostatic interaction of the impinging charged projectile, electron or positron, with nuclear protons and bound electrons. The potential of this interaction at a distance r from the nucleus of the target can be written as

$$V_{st}(r) = ze[\phi_n(r) + \phi_e(r)], \quad (3)$$

where ze is the charge of the projectile. Here, $\phi_n(r)$ and $\phi_e(r)$ are the contributions of the nuclear protons and atomic dressing electrons to this potential. Under static-field approximation, the structure of the target is fully characterized by the spatial charge distributions of bound electrons and that of nuclear protons [25]. Using these density distributions, static potential can now be presented as [26]

$$\phi_n(r) = e \int d\mathbf{r}' \frac{\varrho_n(r')}{|\mathbf{r} - \mathbf{r}'|} \quad \text{and} \quad \phi_e(r) = -e \int d\mathbf{r}' \frac{\varrho_e(r')}{|\mathbf{r} - \mathbf{r}'|}. \quad (4)$$

Here, ϱ_n and ϱ_e are spatial densities of nuclear protons and orbital electrons of the target. These densities are normalized according to

$$\int \varrho(r) 4\pi r^2 dr = \begin{cases} Z - q, & \text{for } \varrho_e \\ Z, & \text{for } \varrho_n \end{cases} \quad (5)$$

with $Z - q$ being the number of dressing electrons and Z , the atomic number of the target. To model the nuclear potential, two-parameter Fermi nuclear density function of the following form [22] is used

$$\varrho_n = \frac{\varrho_0}{e^{(r-R_n)/a} + 1}. \quad (6)$$

Here, the half-density radius $R_n = 4.04435$ fm for the ^{54}Xe nucleus and $a = t/4 \ln 3 = 0.546$ fm with $t = 2.4$ fm being the skin thickness parameter, which is independent of the target. ϱ_0 is normalization constant, determined by equation (5), whose value is twice the proton density at $r = R_n$. Dirac-Fock electron density is generated within the framework of multi-configuration Hartree-Fock technique using Desclaux code [21] in the present work.

Rearrangement collisions between incident electron and target electrons, arising due to their indistinguishability, is a unique feature of electron scattering. This collision is non-local by nature. For an approximate and easy solution of the relativistic equation, the semi-classical local exchange potential [23] of the following form is used

$$V_{ex}(r) = \frac{1}{2}[E - V_{st}(r)] - \frac{1}{2}\{[E - V_{st}(r)]^2 + 4\pi a_0 e^4 \varrho_e(r)\}^{1/2}. \quad (7)$$

Here, E and a_0 are the incident electron energy and the Bohr radius, respectively.

The incoming projectile, while approaching the target, produces uniform electric field over the dimension of target ion for large separation. This electric field induces polarization in the target that acts back on the incoming projectile. This asymptotic potential, independent of the charge of the incoming projectile, can be modeled by the following Buckingham polarization potential

$$V_p(r) = -\frac{\alpha_d e^2}{2(r^2 + d^2)^2}. \quad (8)$$

Here, $\alpha_d = 4.044 \times 10^{-24} \text{ cm}^3$ [27] is the dipole polarizability of xenon atom and d is a phenomenological cut off parameter, which prevents $V_p(r)$ from diverging at $r = 0$ and fits this potential for the required degree of ionicity through the number of dressing electrons ($Z - q$). This parameter can be written as [28]

$$d^4 = \frac{1}{2}\alpha_d a_0 (Z - q)^{-1/3} b_p^2, \quad (9)$$

where b_p is an adjustable energy dependent parameter that decreases with the increase of incident energy and is expressed according to [29] $b_p^2 = \max\{(E - 50 \text{ eV})/(16 \text{ eV}), 1\}$.

When the projectile approaches the target sufficiently closely, the electric field it produces over the dimension of the target ion is no longer uniform and the distortion of the electron cloud becomes different for different projectiles. The asymptotic expansion then completely breaks down and hence interaction potential for the correlation between the projectile and electron cloud is needed to describe this near-target region interaction. Perdew and Zunger gave the following analytic form to describe this interaction for electron [24].

$$V_{co}^{(-)}(r) = -\frac{e^2}{a_0}(0.0311 \ln(r_s) - 0.0584 + 0.00133r_s \ln(r_s) - 0.0084r_s), \quad \text{for } r_s < 1 \quad (10)$$

and

$$V_{co}(r) = -\frac{e^2}{a_0}\beta_0 \frac{1 + (7/6)\beta_1 r_s^{1/2} + (4/3)\beta_2 r_s}{(1 + \beta_1 r_s^{1/2} + \beta_2 r_s)^2} \quad \text{for } r_s \geq 1. \quad (11)$$

Where $\beta_0 = 0.1423$, $\beta_1 = 1.0529$ and $\beta_2 = 0.3334$.

For positrons, the correlation potential as given by Jain [30] is

$$V_{co}^{(+)}(r) = \frac{e^2}{2a_0}\{-1.82r_s^{-1/2} + [0.051 \ln(r_s) - 0.115]\ln(r_s) + 1.167\}, \quad \text{for } r_s < 0.302, \quad (12)$$

$$V_{co}^{(+)}(r) = \frac{e^2}{2a_0}[-0.92305 - 0.09098r_s^{-2}] \quad \text{for } 0.302 \leq r_s < 0.56, \quad (13)$$

and

$$V_{co}^{(+)}(r) = \frac{e^2}{2a_0}\left[-\frac{8.7674}{(r_s + 2.5)^3} + \frac{-13.151 + 0.9552r_s}{(r_s + 2.5)^2} + \frac{2.8655}{(r_s + 2.5)} - 0.6298\right] \quad \text{for } 0.56 \leq r_s < 8.0. \quad (14)$$

For the asymptotic region, $8.0 \leq r_s \leq \infty$, the polarization potential is accurately given by the polarization potential in equation (8). The parameter r_s is given by the following equation

$$r_s \equiv \frac{1}{a_0}\left[\frac{3}{4\pi\varrho_e(r)}\right]^{1/3}. \quad (15)$$

The global CPP is modeled by combining the long range Buckingham potential with the short-range correlation potential as follows [29],

$$V_{cp}^{\pm}(r) \equiv \begin{cases} \max\{V_{co}^{\pm}(r), V_p(r)\} & \text{if } r < r_{cp} \\ V_p(r) & \text{if } r \geq r_{cp}. \end{cases} \quad (16)$$

Where r_{cp} is the outer radius at which $V_{co}(r)$ and $V_p(r)$ cross first.

Projectiles with incident energy greater than the first inelastic threshold are absorbed due to the inelastic channels are opened. An absorptive potential $-iW_{abs}(r)$, which causes a depletion of the projectile wave function, is included with the real potential to account for this effect. A non-relativistic expression of the absorption potential can be obtained under local density approximation (LDA) in the framework of Born-Lindhard formulation, with the Ochkur exchange correction in the case of electrons, as [29]

$$W_{abs}^{nr} = A_{abs} \frac{\hbar}{2} [v_L^{nr} \varrho_e(r) \sigma_{bc}(E_L, \varrho_e, \Delta)]. \quad (17)$$

$\sigma_{bc}(E_L, \varrho_e, \Delta)$ is the total one-electron cross section for binary collisions of the projectile, electron or positron, of non-relativistic velocity [29], $v_L^{nr} = \sqrt{2E_L/m_e}$ corresponding to the local kinetic energy

$$E_L(r) = \begin{cases} E - V_{st}(r) - V_{ex}(r) & \text{for electron} \\ \max\{E - V_{st}(r), 0\} & \text{for positron.} \end{cases} \quad (18)$$

with a degenerate free-electron gas of density ϱ_e involving energy losses larger than the energy gap Δ [29]. This energy gap accounts for the fact that the excitation of the target is possible only when energy lost by the projectile exceeds the first inelastic threshold. For electron scattering, inelastic channels become open above the first excitation energy ϵ_1 . Hence for electron $\Delta = \epsilon_1$. Since positronium formation is often the first inelastic channel to open for positron scattering and the ionization potential, I of xenon is greater than the positronium binding energy 6.8 eV, $\Delta = I - 6.8$ eV for positron scattering. The empirical parameter Δ is thus adopted in this work as

$$\Delta = \begin{cases} \epsilon_1 & \text{for electron} \\ I - 6.8 & \text{for positron.} \end{cases} \quad (19)$$

Here, ϵ_1 is the first excitation energy, I is the ionization potential and 6.8 eV is positronium binding energy. The relativistic generalization of equation (17) can be done by, introducing the relativistic velocity $v_L^r = c\sqrt{E_L(E_L + 2m_e c^2)}/E_L + m_e c^2$, as

$$W_{abs} = \frac{v_L^{nr}}{v_L^r} W_{abs}^{nr} = \sqrt{\frac{2(E_L + m_e c^2)^2}{m_e c^2(E_L + 2m_e c^2)}} \times A_{abs} \frac{\hbar}{2} [v_L^{nr} \varrho_e(r) \sigma_{bc}(E_L, \varrho_e, \Delta)], \quad (20)$$

where, c is the velocity of light in vacuum and A_{abs} is an empirical parameter, which should be of the order of unity. Its value depends on the projectile-target combination and can be determined by fitting the available data. Salvat [29], the propounder of the absorption model used in this work, recommended $A_{abs} = 2$. This value was obtained from the optimization of the fit of experimental DCS data for low (> 1 keV) energy electron scattering off rare gases and mercury atoms. However, there is an option for modification of this value for a better description of the data [25].

2.2. Partial wave analysis

The relativistic Dirac equation for a projectile moving with a velocity v in a central field $V_{mC}(r)$ is given as

$$[c\boldsymbol{\alpha} \cdot \mathbf{p} + \beta m_0 c^2 + V_{mC}(r)]\psi(\mathbf{r}) = (E + m_0 c^2)\psi(\mathbf{r}), \quad (21)$$

with $E + m_0 c^2$ being the total energy of the projectile and the operators $\boldsymbol{\alpha}$ and β , the usual 4×4 Dirac matrices. Solutions of the Dirac equation are the spherical waves and are given by

$$\psi_{E\kappa m}(\mathbf{r}) = \frac{1}{r} \begin{pmatrix} P_{E\kappa}(r) \Omega_{\kappa, m}(\hat{\mathbf{r}}) \\ i Q_{E\kappa}(r) \Omega_{-\kappa, m}(\hat{\mathbf{r}}) \end{pmatrix}, \quad (22)$$

where $P_{E\kappa}(r)$ and $Q_{E\kappa}(r)$ are the upper- and lower-component radial functions and $\Omega_{\kappa, m}(\hat{\mathbf{r}})$ are the spherical spinors. $\kappa = (\ell - j)(2j + 1)$ is the relativistic quantum number with j and ℓ being the total and orbital angular momentum quantum numbers. The radial functions $P_{E\kappa}(r)$ and $Q_{E\kappa}(r)$ of Dirac spherical waves are the solutions of the coupled system of differential equations [31]

$$\frac{dP_{E\kappa}}{dr} = -\frac{\kappa}{r} P_{E\kappa}(r) + \frac{E - V + 2m_0 c^2}{c} Q_{E\kappa}(r) \quad (23)$$

and

$$\frac{dQ_{E\kappa}}{dr} = -\frac{E - V}{c} P_{E\kappa}(r) + \frac{\kappa}{r} Q_{E\kappa}(r). \quad (24)$$

The spherical waves in equation (22) are normalized so that the large-component radial function $P_{E\kappa}(r)$ oscillates asymptotically with unit amplitude and takes the following form

$$P_{E\kappa}(r) \sim \sin\left(kr - \ell \frac{\pi}{2} - \eta \ln 2kr + \delta_\kappa\right). \quad (25)$$

Here, $k = \frac{p}{\hbar} = \frac{\sqrt{E(E + 2m_e c^2)}}{\hbar c}$ is the relativistic wave number of the projectile and $\eta = \frac{qe^2 m_e}{\hbar k}$ is the Sommerfeld parameter. The global phase shift δ_κ , describing the large r behavior of the spherical wave solutions, is given by the following equation

$$\delta_\kappa = \Delta_\kappa + \hat{\delta}_\kappa, \quad (26)$$

with Δ_κ being the Coulomb phase shift of the potential tail and $\hat{\delta}_\kappa$, the complex inner phase shift caused by the complex short-range potential. Dirac-Coulomb phase shift Δ_κ is given by

$$\Delta_\kappa = \arg[\zeta(E + 2m_e c^2) - i(\kappa + \lambda)c\hbar k] - (\lambda - \ell - 1)\frac{\pi}{2} + \arg \Gamma(\lambda + i\eta) - S(\zeta, \kappa)\pi, \quad (27)$$

where, $\zeta = \frac{qe^2}{\hbar\kappa} \approx q\alpha = q/137$, $\lambda = \sqrt{\kappa^2 - \zeta^2}$, and $S(\zeta, \kappa) = 1$ if $\zeta < 0$ and $\kappa < 0$, and $= 0$ otherwise. The phase shift Δ_κ can now be used to obtain the direct and spin flip scattering amplitudes for the scattering of e^\pm from Coulomb potential $V_{coul} = \frac{ze^2}{r}$ as

$$f^{(C)}(\theta) = \frac{1}{2ik} \sum_{\ell=0}^{\infty} \{(\ell + 1)[\exp(2i\Delta_{-\ell-1}) - 1] + \ell[\exp(2i\Delta_\ell) - 1]\} P_\ell(\cos \theta) \quad (28)$$

and

$$g^{(C)}(\theta) = \frac{1}{2ik} \sum_{\ell=0}^{\infty} \{\exp(2i\Delta_\ell) - \exp(2i\Delta_{-\ell-1})\} P_\ell^1(\cos \theta). \quad (29)$$

To calculate the inner phase shifts $\hat{\delta}_\kappa$, the integration of radial equations is started at $r = 0$ and extended outwards up to a distance r_m beyond the effective range of the interaction potential. For $r > r_m$ the potential takes asymptotic Coulombian form and the normalized upper-component radial Dirac function can be written as

$$P_{E\kappa}(r) = \cos \hat{\delta}_\kappa f_{E\kappa}^{(u)}(r) + \sin \hat{\delta}_\kappa g_{E\kappa}^{(u)}(r). \quad (30)$$

$f_{E\kappa}^{(u)}(r)$ and $g_{E\kappa}^{(u)}(r)$ are regular and irregular Dirac-Coulomb functions respectively. The phase shifts $\hat{\delta}_\kappa$ can now be obtained by matching the outer analytical form to the inner numerical solution at r_m . The continuity of the radial function $P_{E\kappa}(r)$ and its derivative is required for this boundary condition. This procedure gives

$$\exp(2i\hat{\delta}_\kappa) = \frac{D_{out}[f_{E\kappa}^{(u)}(r_m) + ig_{E\kappa}^{(u)}(r_m)] - [(f_{E\kappa}^{(u)})'(r_m) + i(g_{E\kappa}^{(u)})'(r_m)]}{[(f_{E\kappa}^{(u)})'(r_m) - i(g_{E\kappa}^{(u)})'(r_m)] - D_{out}[f_{E\kappa}^{(u)}(r_m) - ig_{E\kappa}^{(u)}(r_m)]}, \quad (31)$$

where the primes indicate the derivatives with respect to r and D_{out} , the logarithmic derivative of the outgoing numerical radial function at the matching point. The complex form of the phase shift $\hat{\delta}_\kappa$ is due to the complex short-range potential $V_{sr}(r)$ in equation (2). The scattering amplitudes $f_{sr}(\theta)$ and $g_{sr}(\theta)$, for the short-range potential, are given as

$$f_{sr}(\theta) = \frac{1}{2ik} \sum_{\ell=0}^{\infty} \{(\ell + 1)\exp(2i\Delta_{-\ell-1})[\exp(2i\hat{\delta}_{-\ell-1}) - 1] + \ell \exp(2i\Delta_\ell)[\exp(2i\hat{\delta}_\ell) - 1]\} P_\ell(\cos \theta) \quad (32)$$

and

$$g_{sr}(\theta) = \frac{1}{2ik} \sum_{\ell=0}^{\infty} \{\exp(2i\Delta_\ell)[\exp(2i\hat{\delta}_\ell) - 1] - \exp(2i\Delta_{-\ell-1})[\exp(2i\hat{\delta}_{-\ell-1}) - 1]\} P_\ell^1(\cos \theta). \quad (33)$$

The scattering of e^\pm by the modified Coulomb potential can be designated by the following direct and spin flip scattering amplitudes $f(\theta)$ and $g(\theta)$

$$f(\theta) = f^{sr}(\theta) + f^C(\theta), \quad g(\theta) = g^{sr}(\theta) + g^C(\theta). \quad (34)$$

These scattering amplitudes are used to calculate the elastic DCS per unit solid angle and IECS for unpolarized e^\pm by the following respective expressions.

$$\frac{d\sigma}{d\Omega} = |f(\theta)|^2 + |g(\theta)|^2. \quad (35)$$

and

$$\sigma_{el} = \int \frac{d\sigma}{d\Omega} d\Omega = 2\pi \int_0^\pi (|f(\theta)|^2 + |g(\theta)|^2) \sin(\theta) d\theta. \quad (36)$$

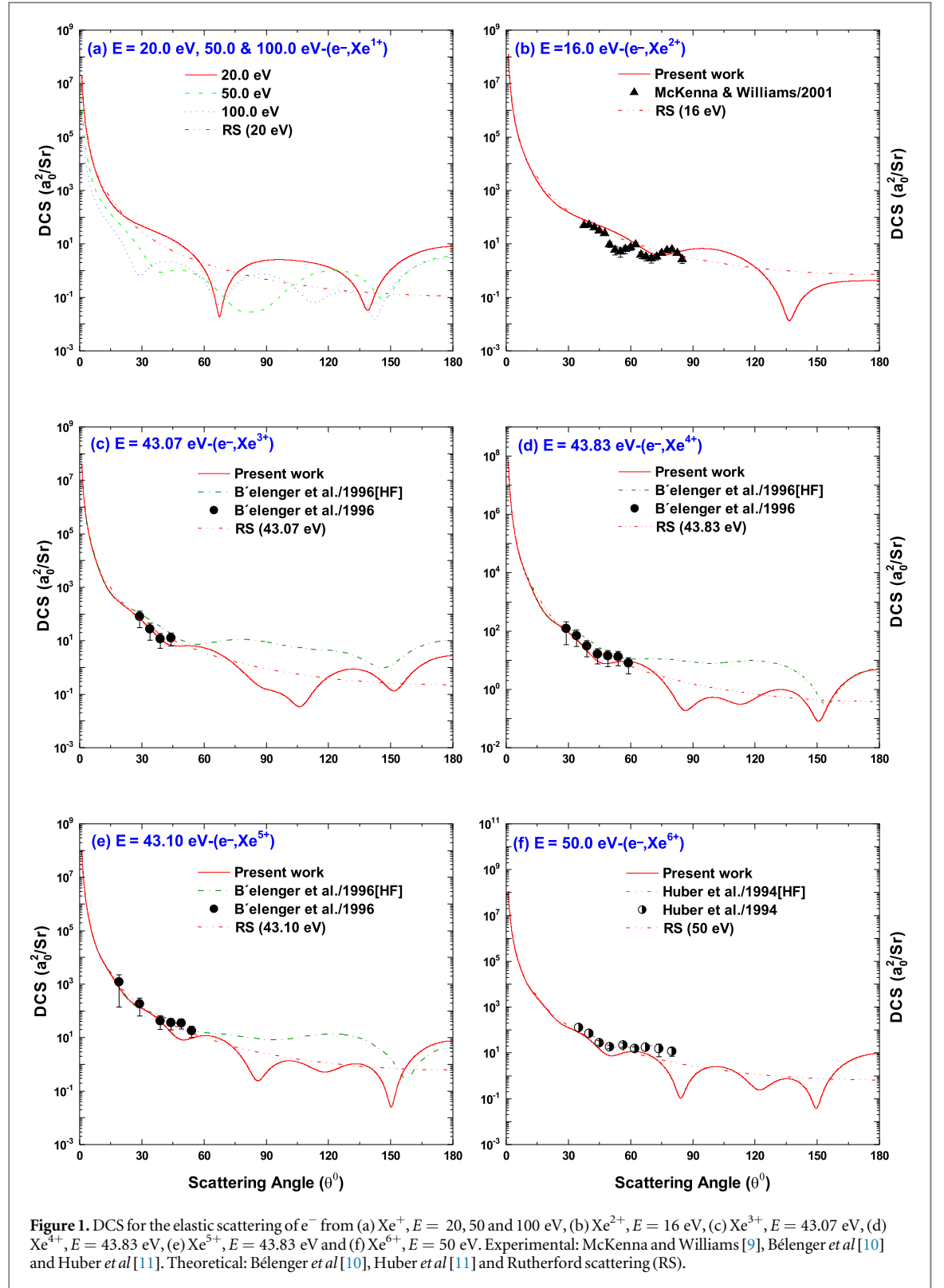
The following equation is used to calculate the momentum transfer cross section (MTCS), which is a measure of the average momentum transferred per collision from the projectile to the target ion

$$\sigma_m = 2\pi \int_0^\pi (1 - \cos \theta)(|f(\theta)|^2 + |g(\theta)|^2) \sin(\theta) d\theta. \quad (37)$$

DCS per unit solid angle for the elastic scattering of electron by the bare xenon is calculated according to

$$\frac{d\sigma}{d\Omega} = |f^C(\theta)|^2 + |g^C(\theta)|^2. \quad (38)$$

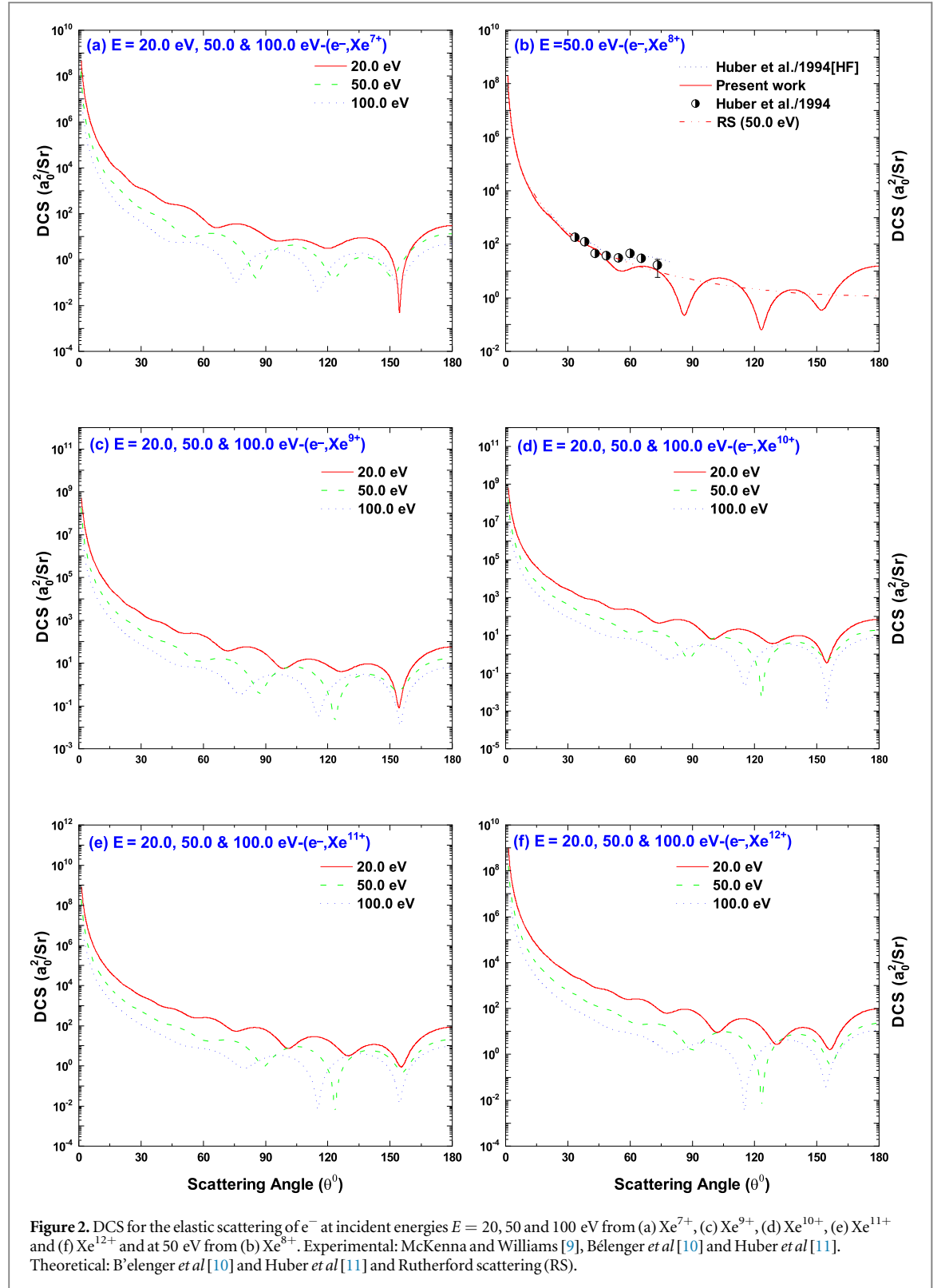
The initially unpolarized electron or positron beam becomes polarized after being scattered in the direction θ . The degree of this spin polarization is given by Sherman function [32]



$$S(\theta) \equiv i \frac{f(\theta)g^*(\theta) - f^*(\theta)g(\theta)}{|f(\theta)|^2 + |g(\theta)|^2}. \quad (39)$$

To present a quantitative measure of the Coulomb glory effect, DCS in equation (35) has been scaled according to [33]

$$\frac{d\tilde{\sigma}}{d\Omega} = \left(\frac{4E}{q} \right)^2 \frac{d\sigma}{d\Omega} \quad (40)$$

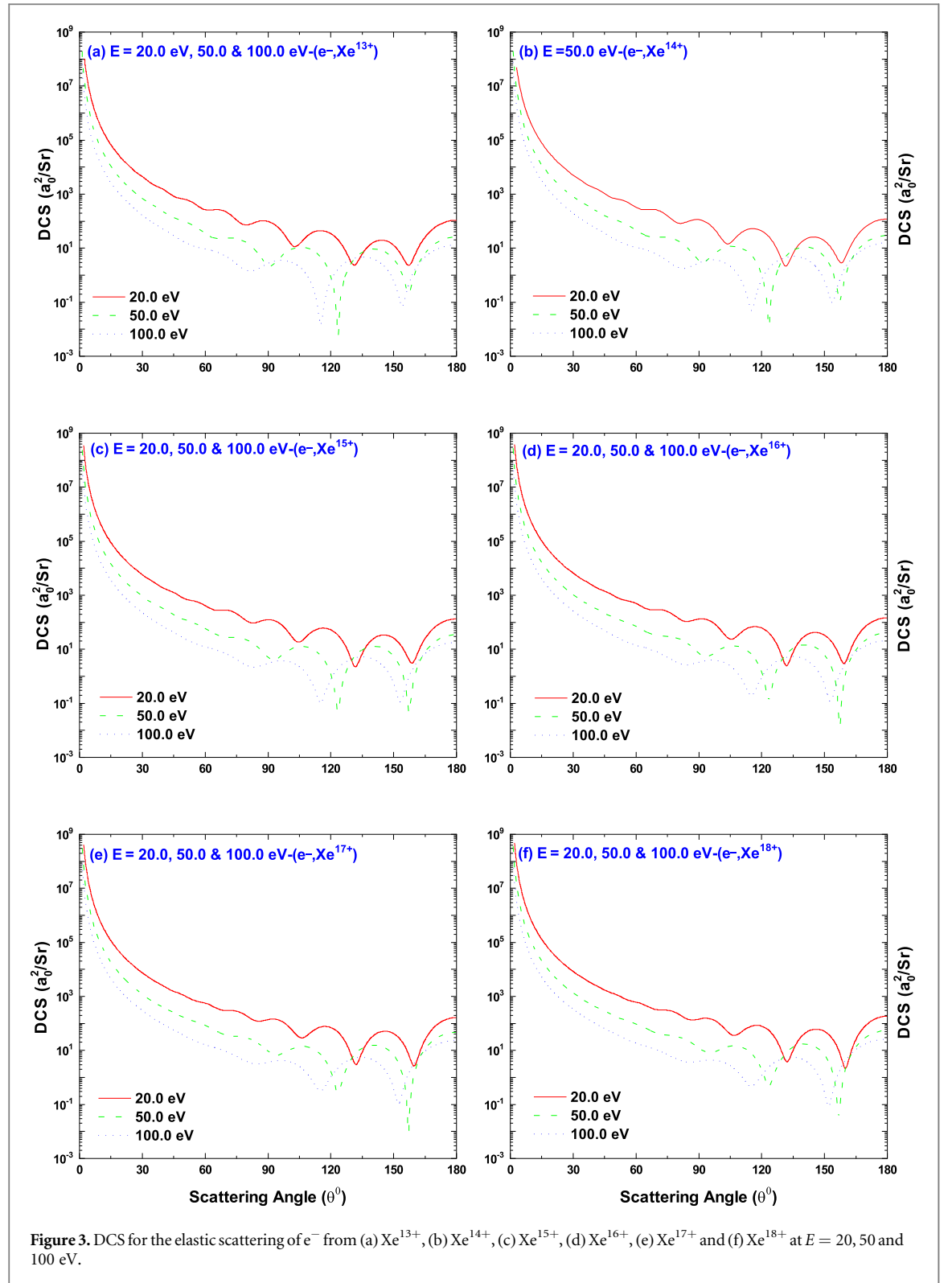


The scaled Rutherford differential cross section (SRCS), independent of energy and ionic charge, is given as

$$\frac{d\tilde{\sigma}^c}{d\Omega} = \frac{1}{\sin^4 \theta/2}. \quad (41)$$

The value of SRCS is unity at 180° and hence the scaled differential cross section (SDCS), $\frac{d\tilde{\sigma}}{d\Omega}$ in equation (40) represents the ratio of e^- -ion DCS and corresponding Rutherford DCS at $\theta = 180^\circ$.

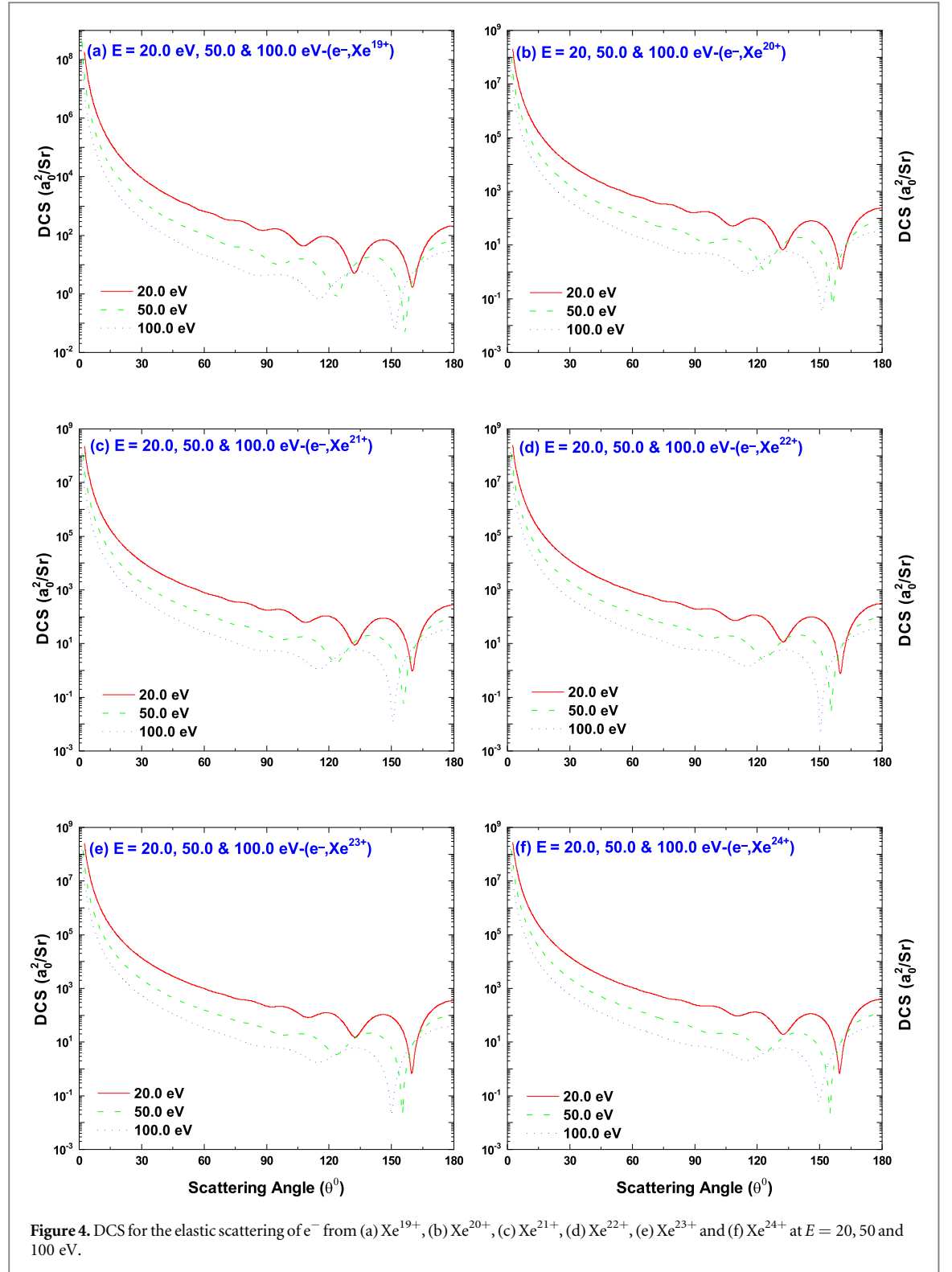
The partial-wave series converge very slowly for the small angle elastic scattering by ions. There is scope for 25 000 partial waves. Angular momentum is increased up to a certain maximum for which the absolute value of the phase-shift is less than 10^{-9} . At this point partial wave expressions for $f(\theta)$ and $g(\theta)$ converge to the required



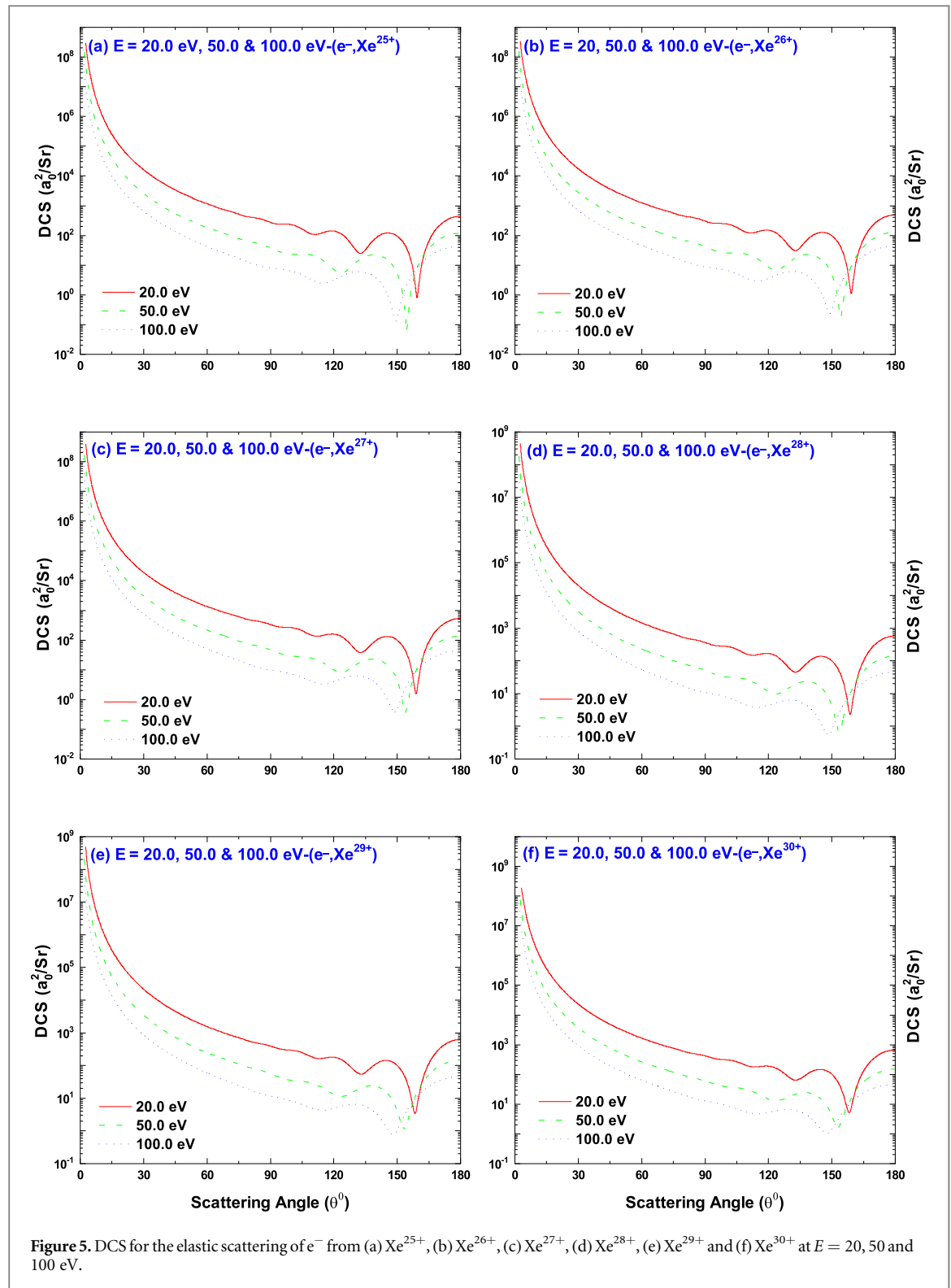
accuracy (usually more than six decimal places) for all angles. In the calculations of scattering amplitudes and cross sections, scattering angles larger than 1° are considered to avoid the divergence [25].

3. Results and discussions

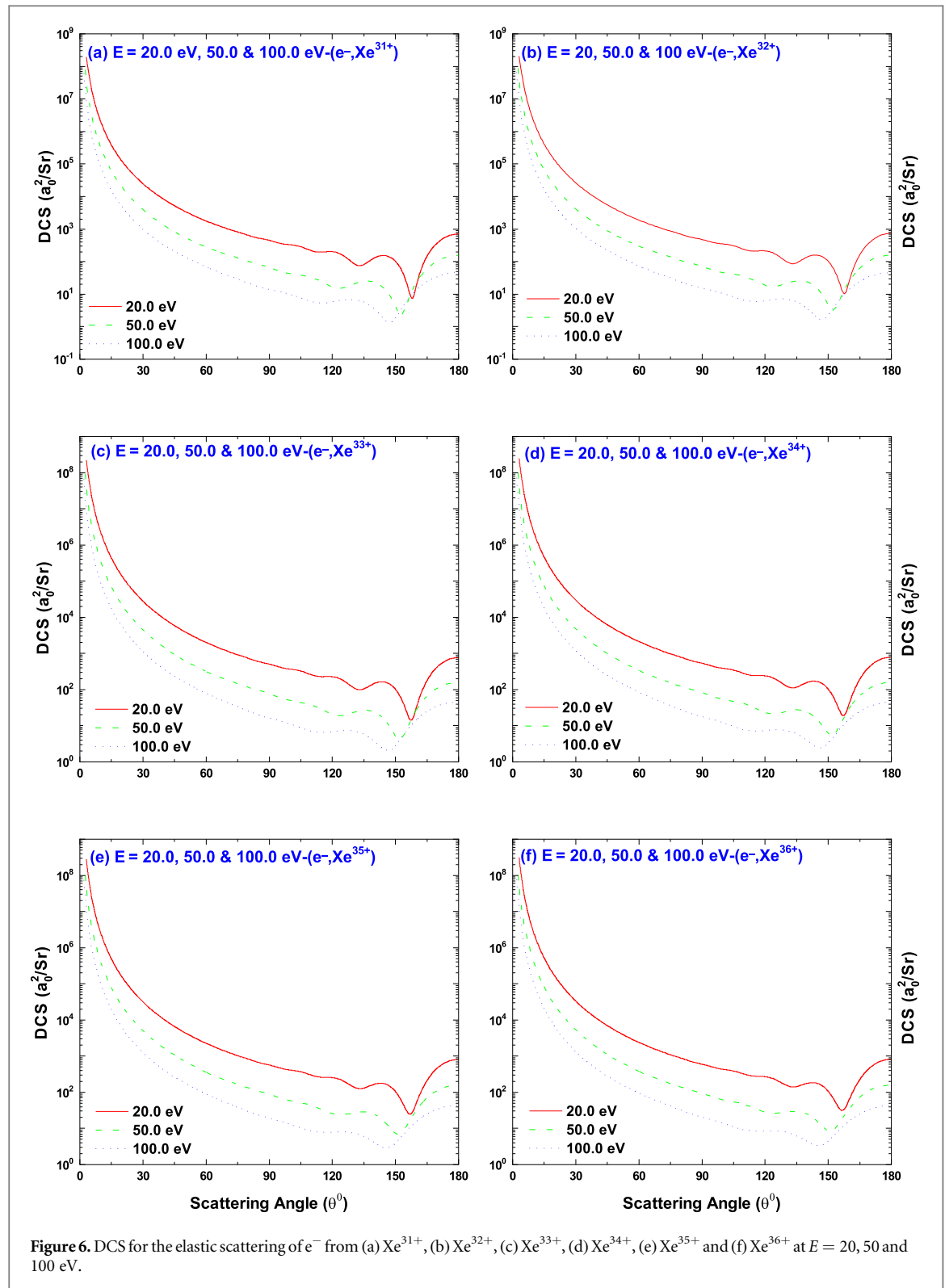
This investigation involves the calculations of DCS, IECS, MTCS and Sherman function for $e^\pm-Xe^{q+}$ scattering using modified Coulomb potential within the framework of Dirac relativistic partial wave analysis using ELSEPA code [25]. Predicted observable quantities of our work are presented in comparison with the available experimental data [9–11] and other theoretical predictions [10, 11].



In figure 1(a), we present DCSs at 20, 50 and 100 eV and Rutherford scattering cross section (RS) at 20 eV for the scattering of electron from Xe^+ . In figure 1(b), we compare our calculated DCS for $e^- - Xe^{2+}$ with the experimental data of McKenna and Williams [9] and the corresponding RS. Two shallow minima are observed in the experimental DCS, one at $\sim 55^\circ$ and another at $\sim 70^\circ$. Our method cannot reproduce the first minimum but can predict the second one at $\sim 75^\circ$. Oscillations in experimental data [9] is observed to take place from $\sim 50^\circ$ while those start at $\sim 70^\circ$ in our OPM predicted DCS. The deviation of our OPM result from Rutherford behavior is not unexpected. In figure 1(c), we depict our DCS results for Xe^{3+} along with the experimental measurement, Hartree-Fock calculations of Bélenger *et al* [10] and Rutherford scattering. A good agreement is observed between our results and the experimental data. Our predicted interference minimum at $\sim 47^\circ$ is closer

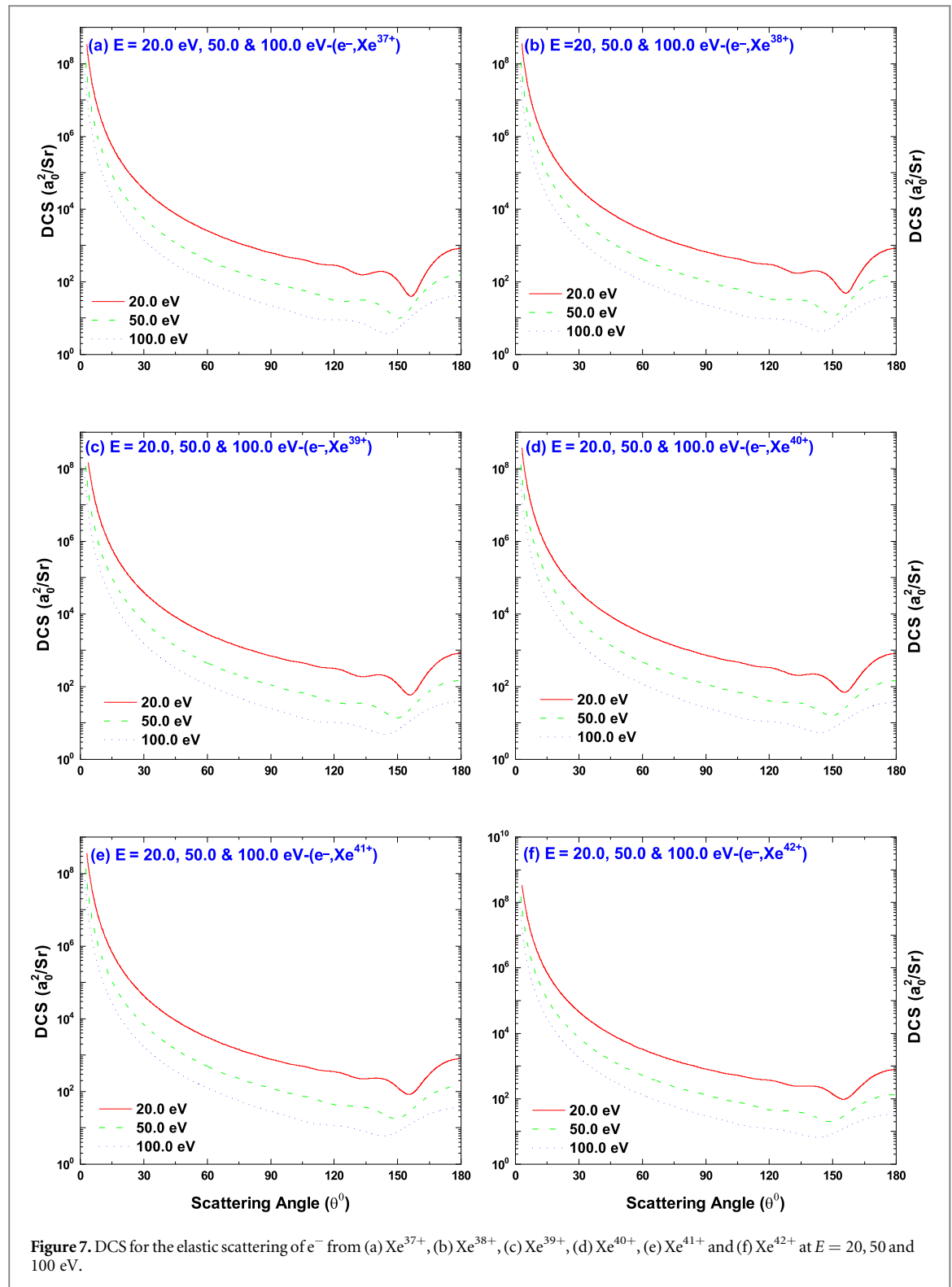


to the experimental minimum at $\sim 39^\circ$ than the Hartree-Fock predicted minimum at $\sim 59^\circ$. These two calculations do not agree with each other in the angular range $\sim 70^\circ - 140^\circ$ both in magnitude and pattern. This difference between the results is might be caused due to different procedures of calculations. In figures 1(d) and (e), the above two calculations show almost similarity in agreement with each other and with the experimental data as in figure 1(c) although the calculations of Bélenger *et al* [10] show a better agreement with their experimental data in figure 1(e). In figure 1(f), our predictions are in reasonable agreement with the experimental measurement [11] while the Hartree-Fock calculations [11] show a little better agreement than ours. From figures 1(c)–(f), it is observed that deviation of measured data from Rutherford scattering starts at $\sim 50^\circ$, which is well predicted by our method. It is evident from the figures that the degree of ionicity does have

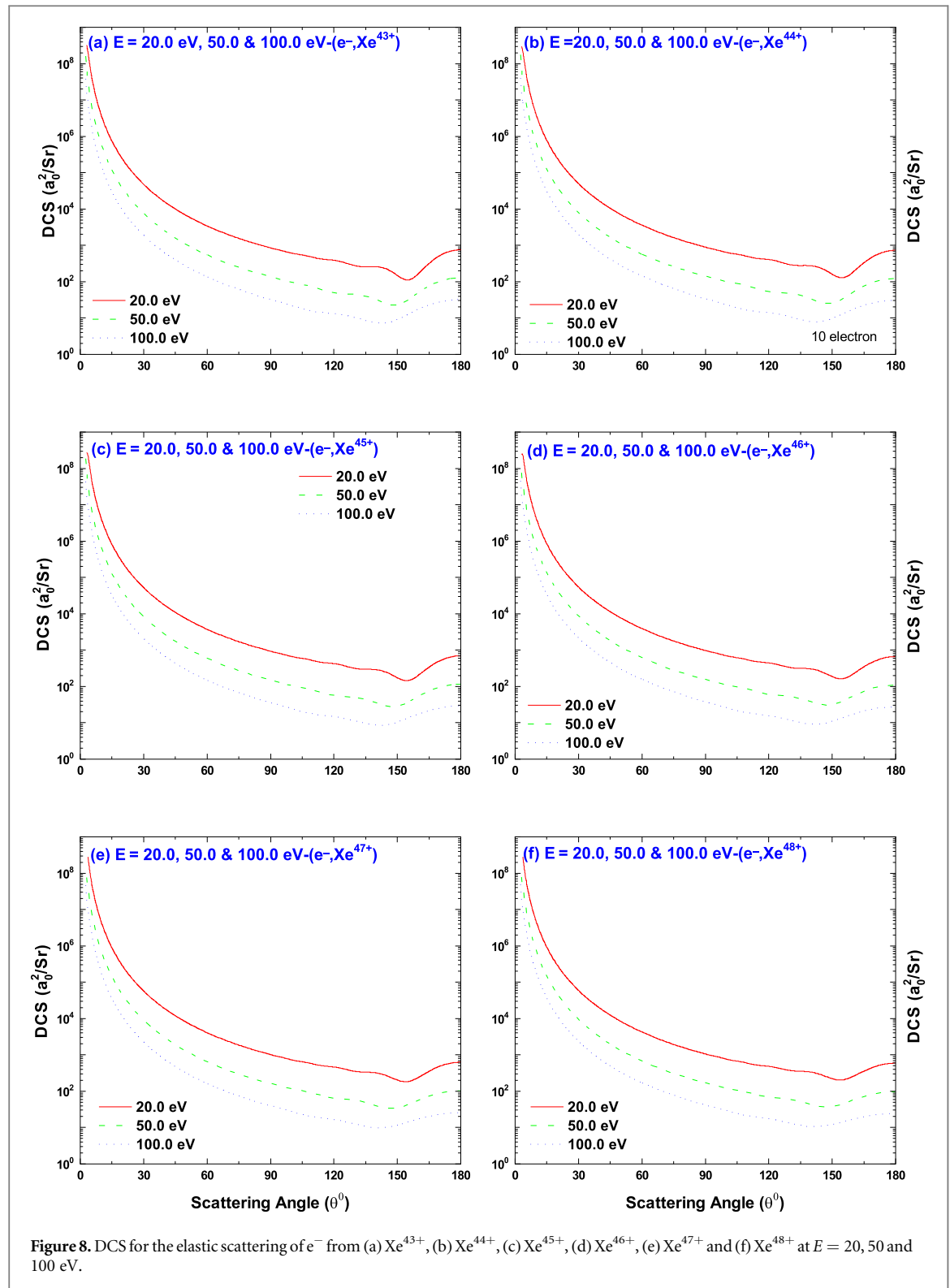


effect on the DCS pattern because of the difference of the number of electrons involved in the scattering. In figure 2(b), we compare our DCS result for Xe^{8+} with the Hatree-Fock calculations of Huber *et al* [11] and the corresponding Rutherford scattering (RS). Our calculations show reasonable agreement with the measured data. The smooth variation of RS, in disagreement with above two calculations, is due to scattering from bare nucleus without the shielding effect of bound electrons the scatterings from which form an interference pattern of maxima and minima.

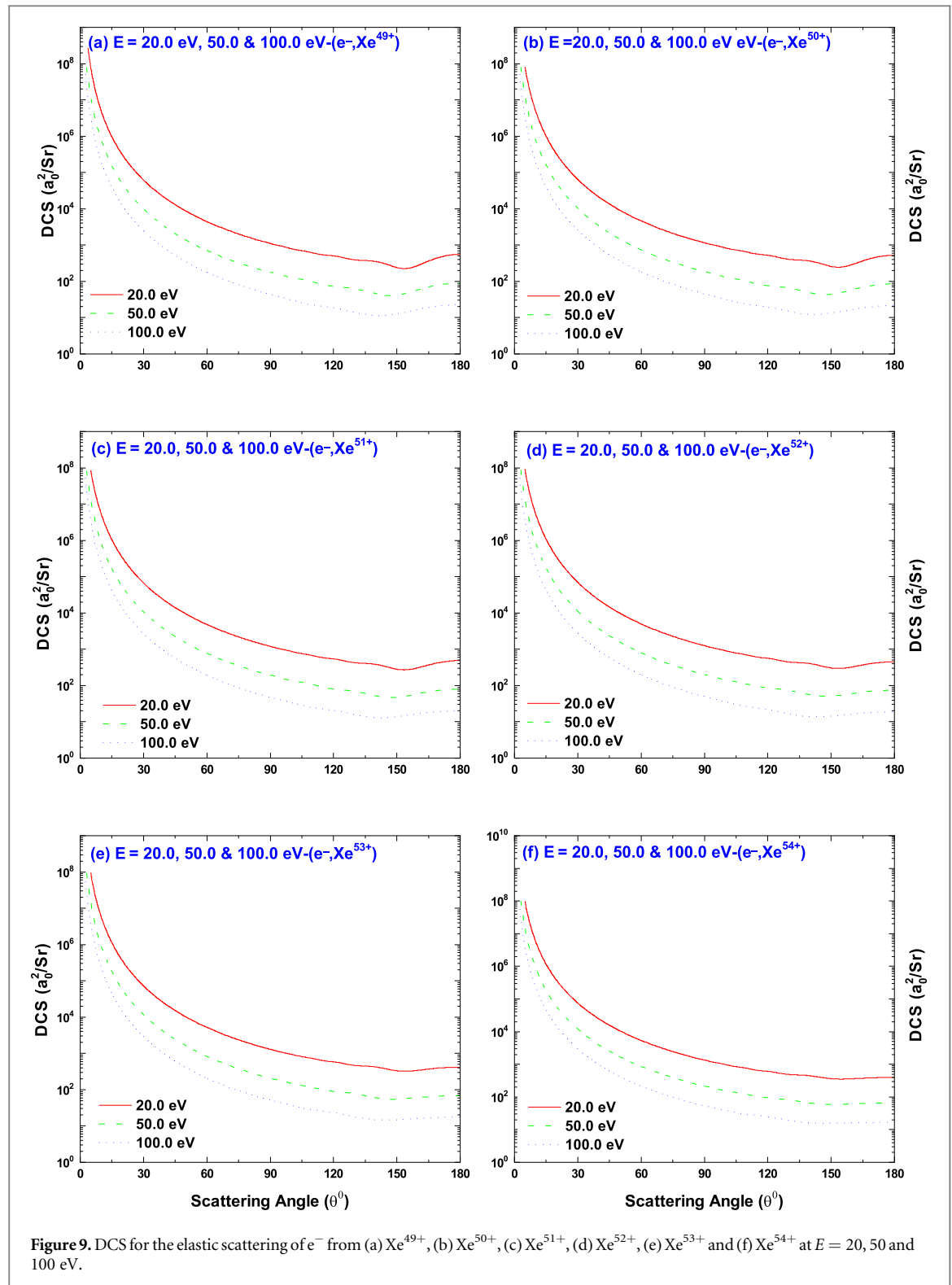
We show our predicted DCS at energies 20, 50 and 100 eV for the elastic scattering of electron from Xe^{7+} - Xe^{12+} in figure 2 and those from Xe^{13+} - Xe^{53+} in figures 3–9. It is observed from these figures that, for a particular charge state, increasing energy shifts the interference minimum towards lower angles. A rise in DCS



with the increase of the ionic state is also observed at a specific angle and energy. Airy interference structure is prominently observed at large scattering angles in the angular distribution of cross sections for the scattering of low energy electron from ions of low and intermediate degrees of ionicities (figures 2–6). Coherent interference of the waves scattered due to short-range and asymptotic Coulomb forces causes this manifestation of sharp structure in DCS. When the velocity of bound electrons is comparable to that of projectile electron, the short-range potential can provide enhanced electron-electron correlation for small orbital angular momentum (impact parameter). Scattering amplitudes due to this prominent short-range force and those due to asymptotic Coulomb force interfere coherently. This coherent interference, a reflection of core penetration of projectile electron, is manifested as sharp structure in the angular distribution. This Airy structure does not have



noteworthy appearance in DCS of electrons scattered elastically from the ions of isonuclear series of low or intermediate atomic number [3, 12, 19]. Prominent short-range interaction, emerging due to the large number of dressing electrons of xenon ions of low and intermediate ionicities, contribute to this Airy structure. It is observed that this interference structure declines with the fall of the number of atomic electrons (figures 2–9). This observation is affirmed by the experimental data [10, 34]. But in case of xenon, increasing the degree of ionicity causes slow depletion of atomic electrons due to its large atomic number. This in turn allows the short-range potential to maintain its dominance over the Coulomb potential with the increase of ionicity. As a result, the disappearance of interference structure for a heavy target occurs gradually (figures 2–6). Hence Coulomb domination over the short-range potential takes place slowly with the increase of charge states for a heavy target,



like xenon. In case of medium and light target, this domination in angular distribution takes place rapidly with the increase of ionicities. It is also observed that the pronounced interference structure observed for the scattering of electron off the low ionic states tends to become weaker with the increase of projectile energy (figures 2 and 10). Incoherent interference of greater number of angular momentum waves causes this weakening. In figure 9(f), we illustrate the angular distribution of elastic scattering of electron from bare xenon. The DCS at all incident energies and charge states across the isonuclear series at $\theta = 0^\circ$ diverges in Rutherford prediction. This divergence is removed by modified Coulomb field due to the screening of the bound electrons, but the maximum in DCS is retained at this angle. The interference of the incident wave and forward scattering amplitude produces this maximum in and around $\theta = 0^\circ$.

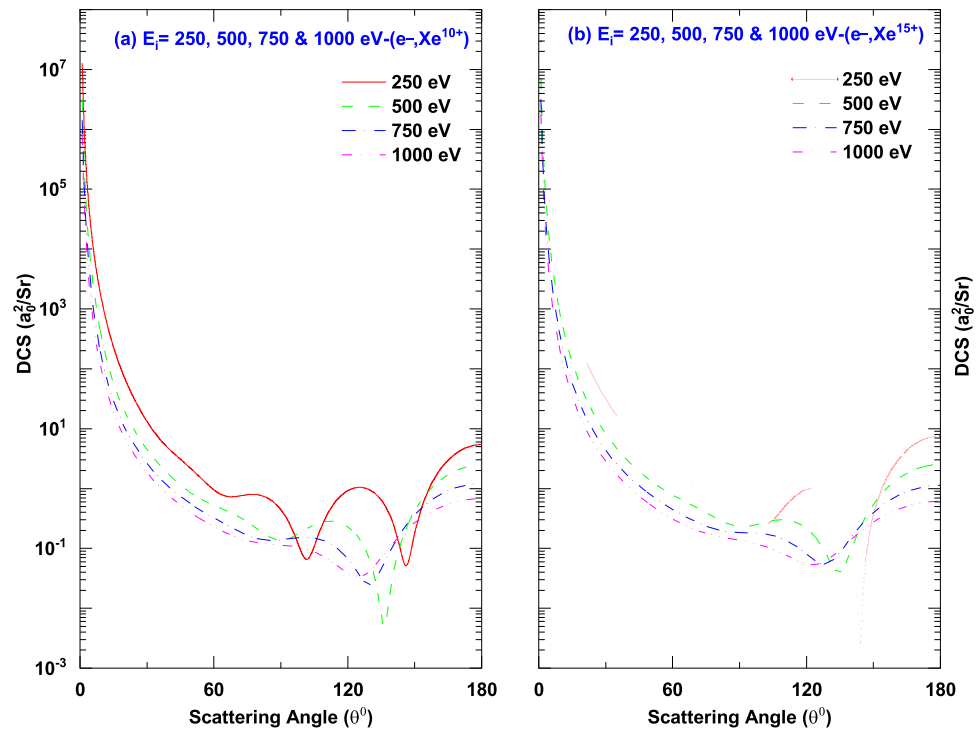


Figure 10. DCS for the elastic scattering of e^- from (a) Xe^{10+} and (b) Xe^{15+} at $E = 250, 500, 750$ and 1000 eV.

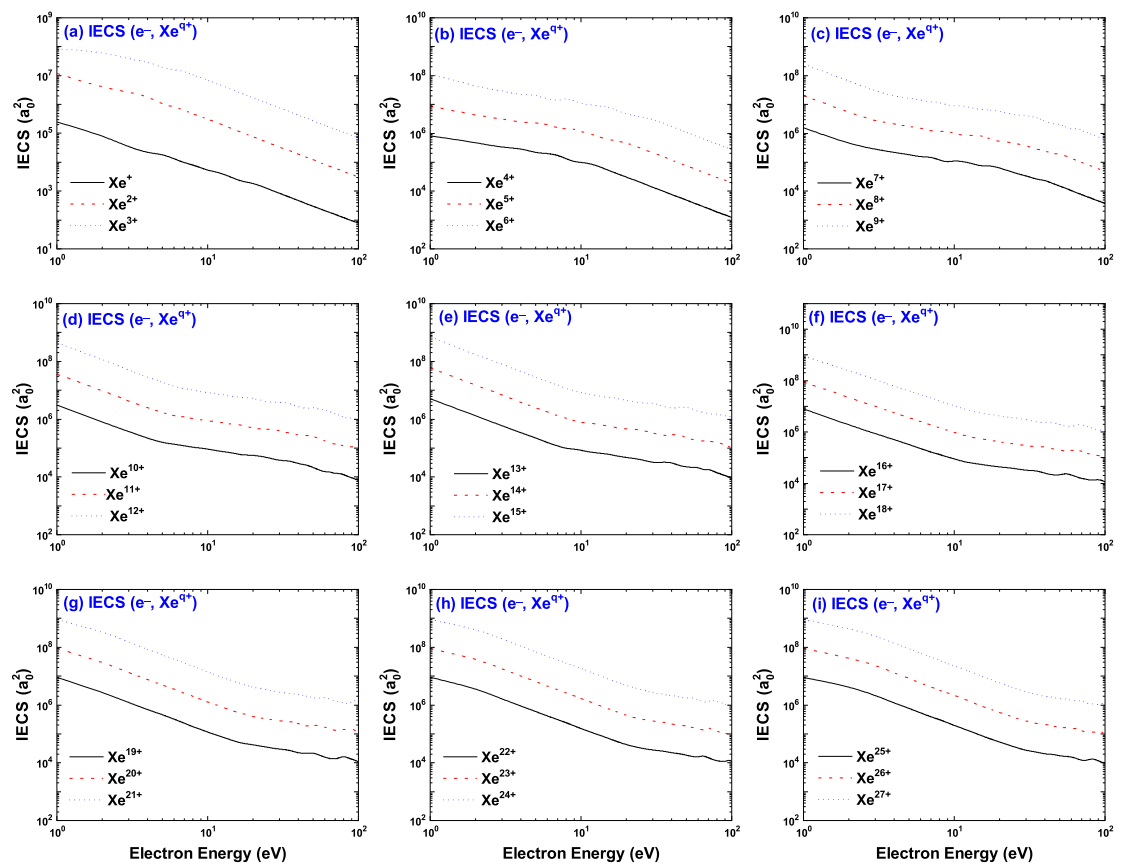
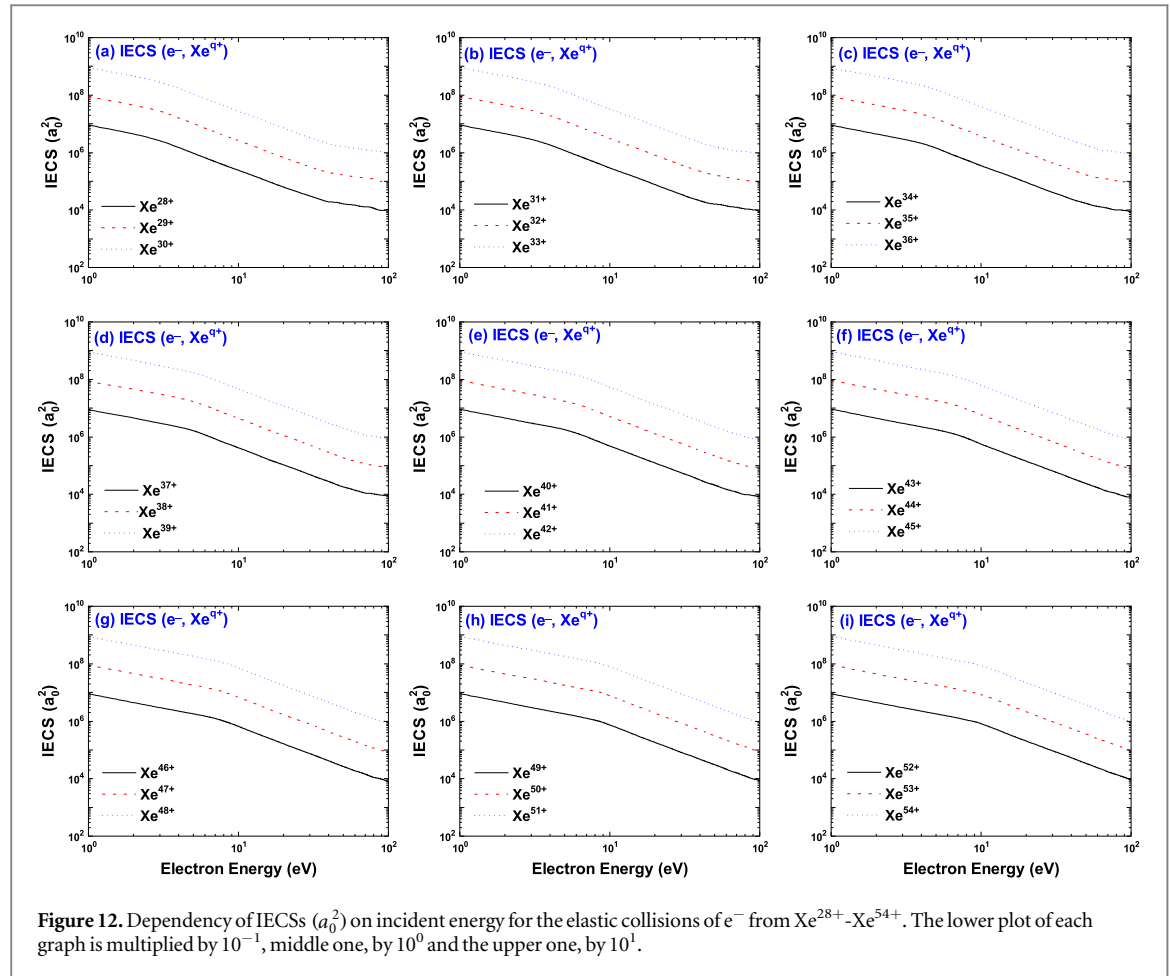


Figure 11. Dependency of IECs (a_0^2) on incident energy for the elastic collisions of e^- from Xe^+ - Xe^{27+} . The lower plot of each graph is multiplied by 10^{-1} , middle one, by 10^0 and the upper one, by 10^1 .



In figures 11 and 12, we present our predictions for the IECs. An increase in IECs with the increase of charge states is observed up to the degree of ionicity $q = 18$. This increase is due to the diminution of screening effect of the dressing electrons. For the ions Xe^{19+} - Xe^{54+} , IECs remain almost unchanged with the increase of charge state. Increasing ionicity mitigates the role of the screening and hence the total cross section is almost exclusively determined by the potential due to nuclear charge distribution. However, the screening effect is manifest in DCS. Our MTCS calculations, presented in figures 13 and 14, show the aforesaid trend observed for IECs due to the aforesaid reason.

In figure 15, we present the scaled differential cross section (SDCS) as a function of scattering angle θ according to equation (40) and scaled Rutherford cross section (SRCS) according to equation (41). A maximum is observed at $\theta = 180^\circ$. This maximum indicates the presence of Coulomb glory that arises due to the electrostatic screening of nuclear potential by atomic electrons. Most prominent effects are observed at the incident energies 425, 200 and 95 eV for the scattering of electrons off the ions of ionicities 20^+ , 30^+ and 40^+ respectively. At a particular critical energy and ionicity, the effect is less pronounced for other higher and lower incident energies. It is evident that with the increase of ionicity the strongest Coulomb glory shifts toward low incident energy. Strength of the potential of the electronic cloud at the origin is stronger for lower degree of ionicities than higher ones. Hence, ion target of high ionicity can cause low energy electron to get backscattered and vice versa. This causes strongest Coulomb glory to be observed at low incident energy for ion of higher ionicity and at comparatively high incident energy for ion of low ionicity. For a particular charge state, the width of the maximum increases with the increase of energy and for a particular ionicity, the ratio of ion DCS to Rutherford DCS decreases with the increase of ionicity. We present the Coulomb glory for argon ($q = 5^+$, 10^+ , 15^+) and neon ($q = 4^+$, 6^+ , 8^+) in figures 16(a)–(c) and (d)–(f) respectively. The same aforesaid features are observed for these two cases. It is evident that at a particular energy the width of the strongest maximum increases and the ratio of ion DCS to Rutherford DCS decreases with the decrease of atomic number, i.e., the maximum flatten with the increase of atomic number. We also present Coulomb glory for the isonuclear series of xenon, argon and neon in figures 17, 18(a)–(c) and (d)–(f) respectively. The features observed in figure 17 are similar to those observed in figure 15. But in case of argon and neon, a smooth decrease of the ratio of ion DCS to Rutherford DCS is observed instead of getting pronounced effect at a particular critical energy and ionicity. It is evident from figures 1–9 and 15–16 that there is an interconnection between the abatement of interference

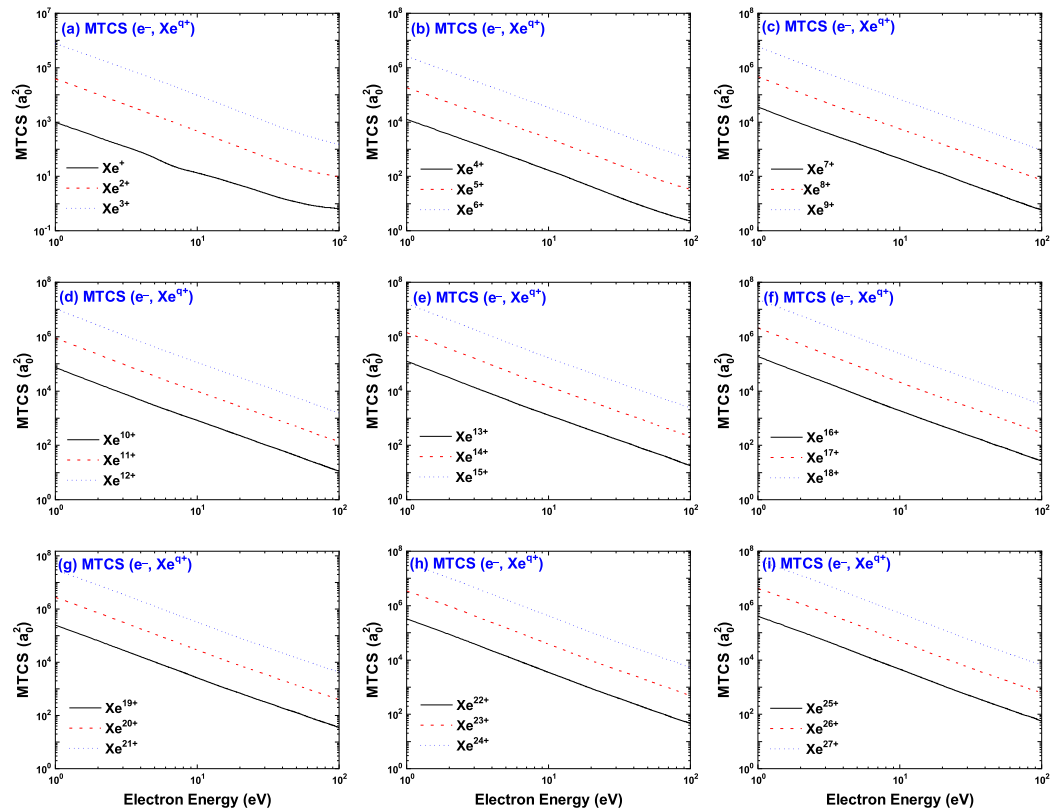


Figure 13. Dependency of MTCSs (a_0^2) on incident energy for the elastic collisions of e^- from Xe^+ - Xe^{27+} . The lower plot of each graph is multiplied by 10^{-1} , middle one, by 10^0 and the upper one, by 10^1 .

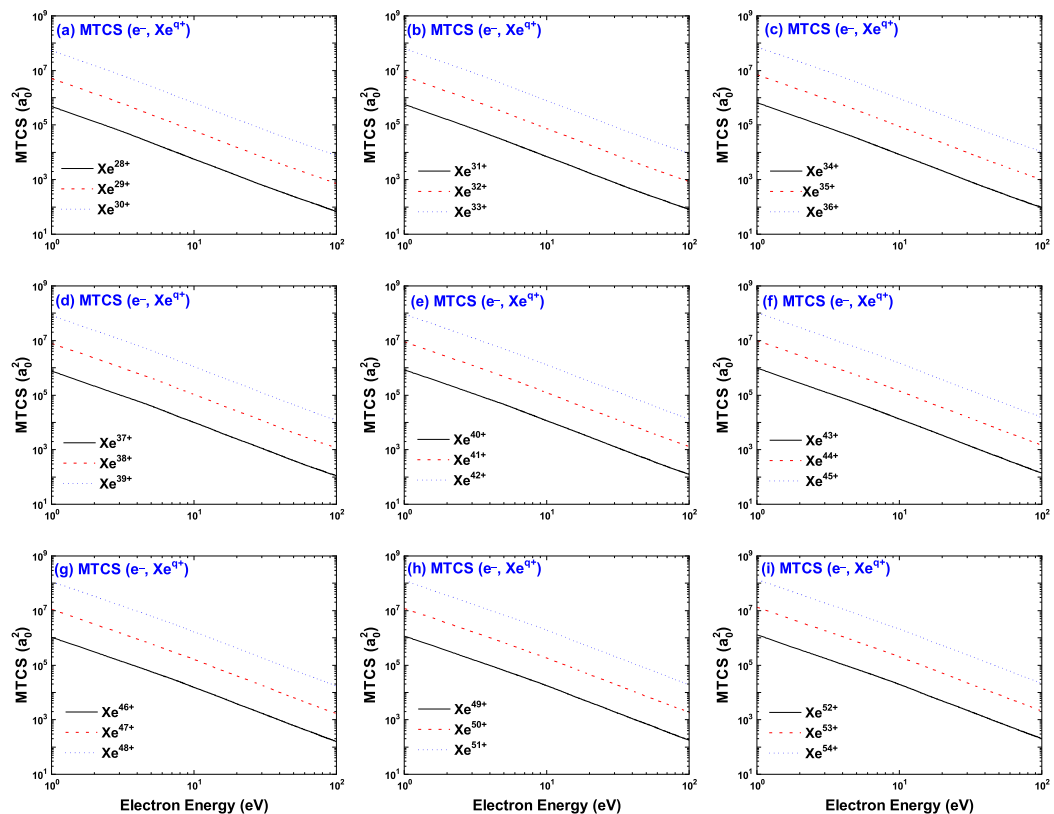


Figure 14. Dependency of MTCSs (a_0^2) on incident energy for the elastic collisions of e^- from Xe^{28+} - Xe^{54+} . The lower plot of each graph is multiplied by 10^{-1} , middle one, by 10^0 and the upper one, by 10^1 .

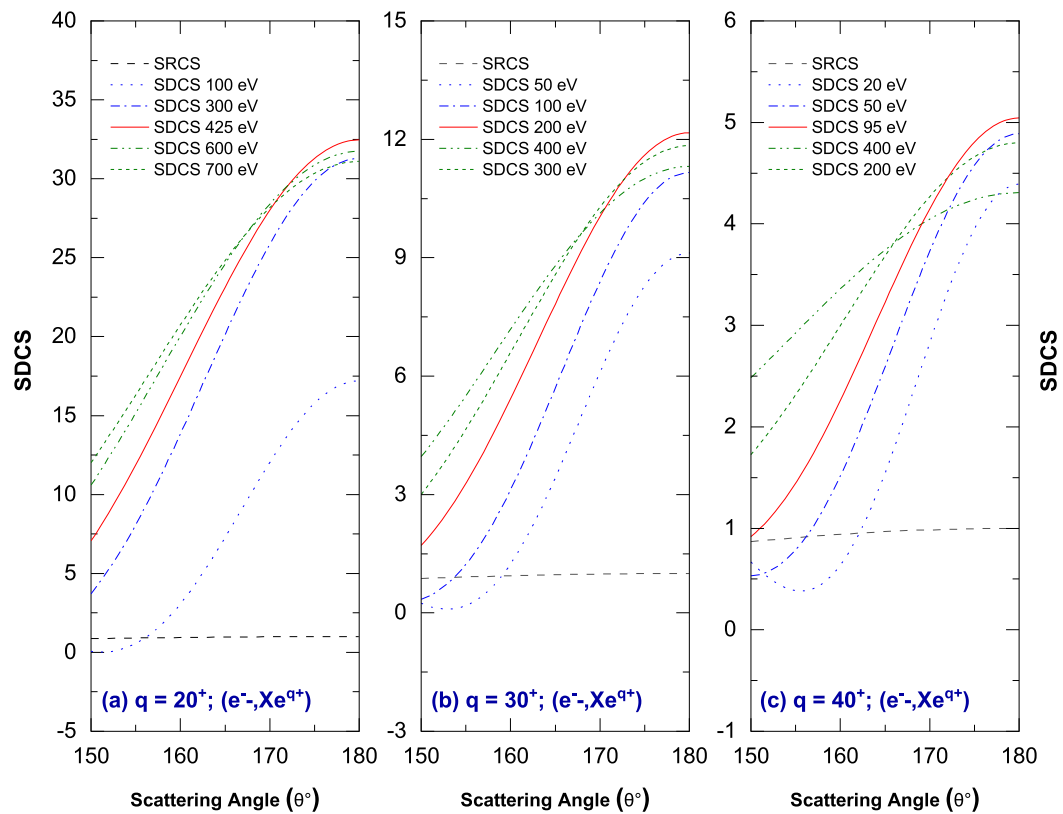


Figure 15. SDCS according to equation (40) at different energies for the ionicities (a) $q = 20^+$, (b) $q = 30^+$ and (c) $q = 40^+$ for (e^- - Xe^{q+}) scattering and the SRCS [dash line] for the same scattering system.

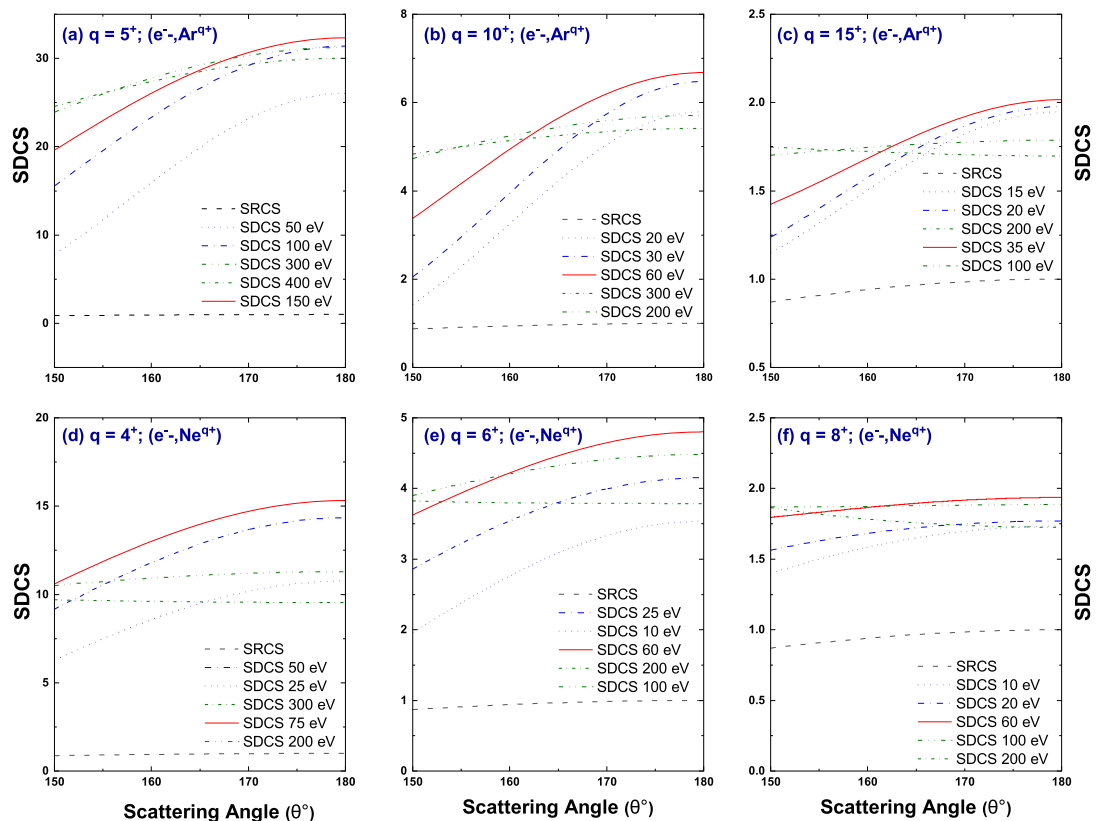


Figure 16. SDCS according to equation (40) at different energies for the ionicities (a) $q = 5^+$, (b) $q = 10^+$ and (c) $q = 15^+$ for (e^- - Ar^{q+}) and (d) $q = 4^+$, (e) $q = 6^+$ and (f) $q = 8^+$ for (e^- - Ne^{q+}) scattering. Dash line represents corresponding SRCS.

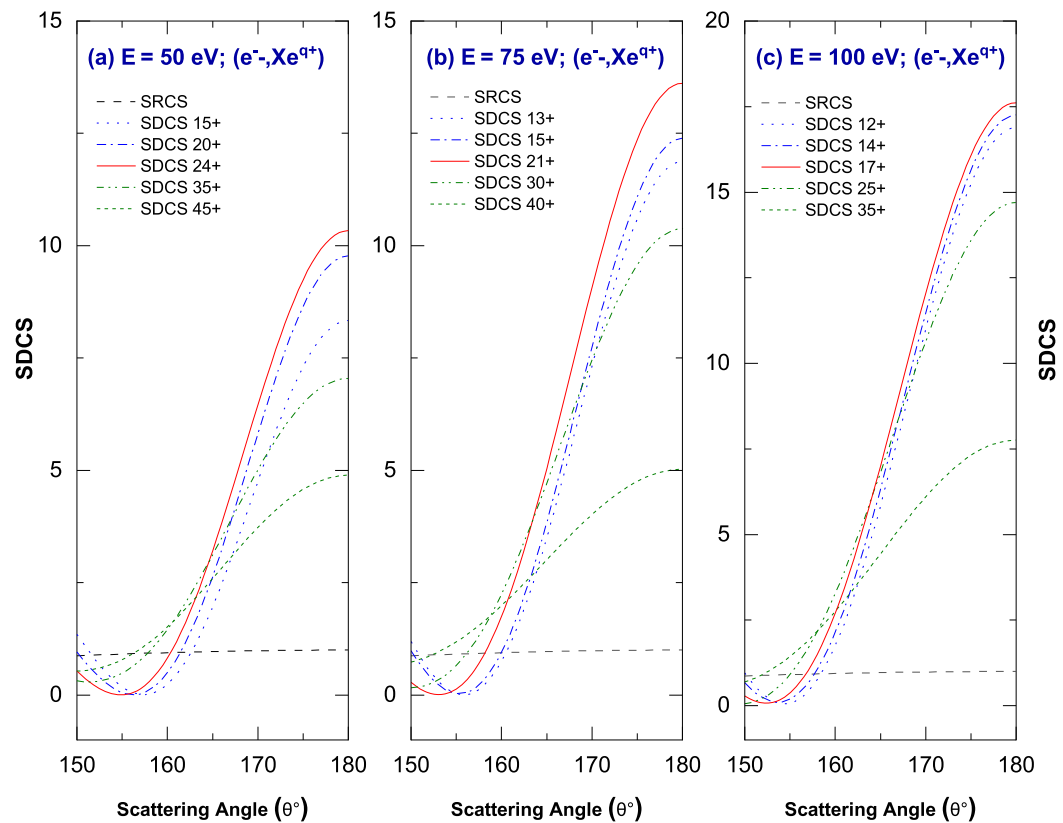


Figure 17. SDCS according to equation (40) for different charge states at the incident energies (a) $E = 50$ eV, (b) $E = 75$ eV and (c) $E = 100$ eV for e^- -Xe $^{9+}$ scattering and the SRCS [dash line] for the same scattering system.

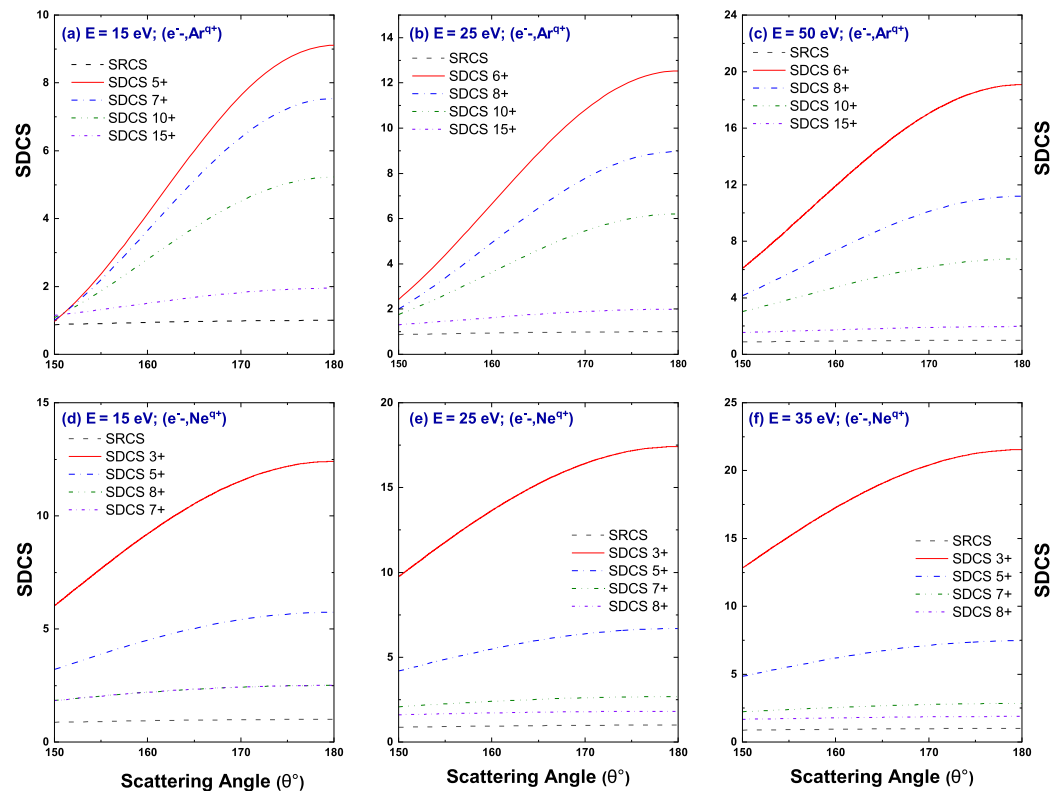
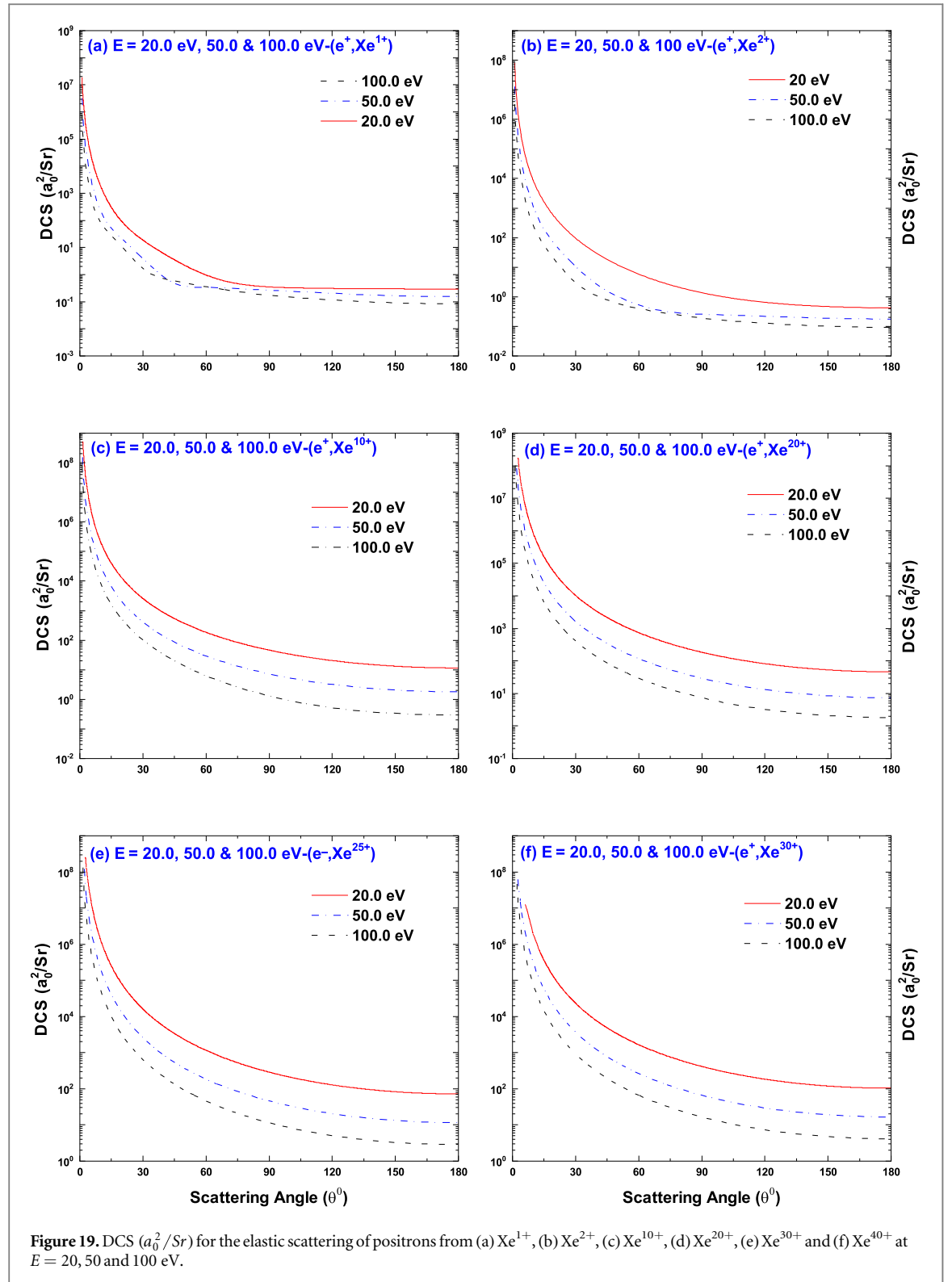
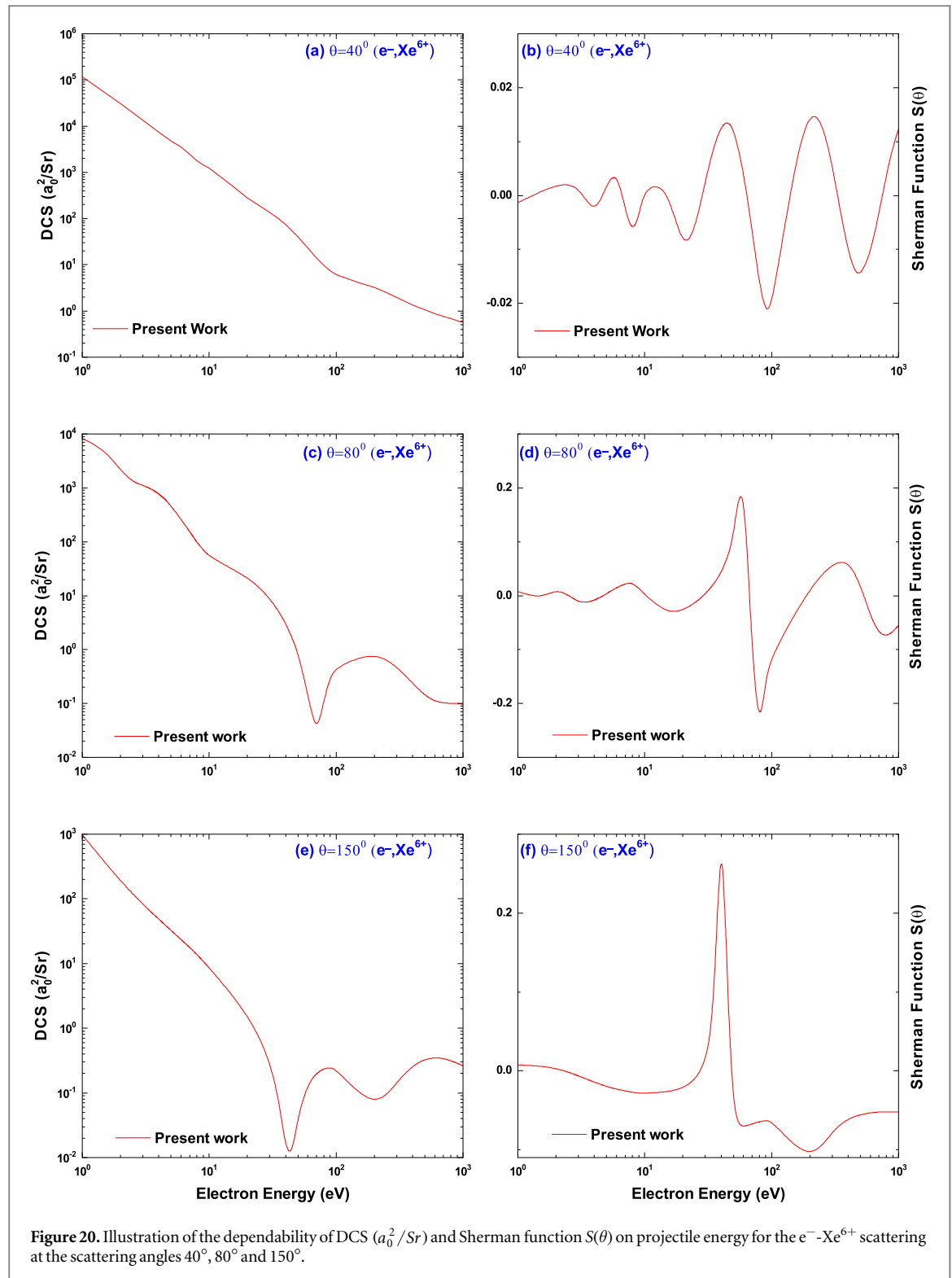


Figure 18. SDCS according to equation (40) for different charge states at the incident energy (a) $E = 15$ eV, (b) $E = 25$ eV and (c) $E = 50$ eV for e^- -Ne $^{9+}$ and (d) $E = 15$ eV, (e) $E = 25$ eV and (f) $E = 35$ eV for e^- -Ar $^{9+}$ scattering. Dash line represents corresponding SRCS.

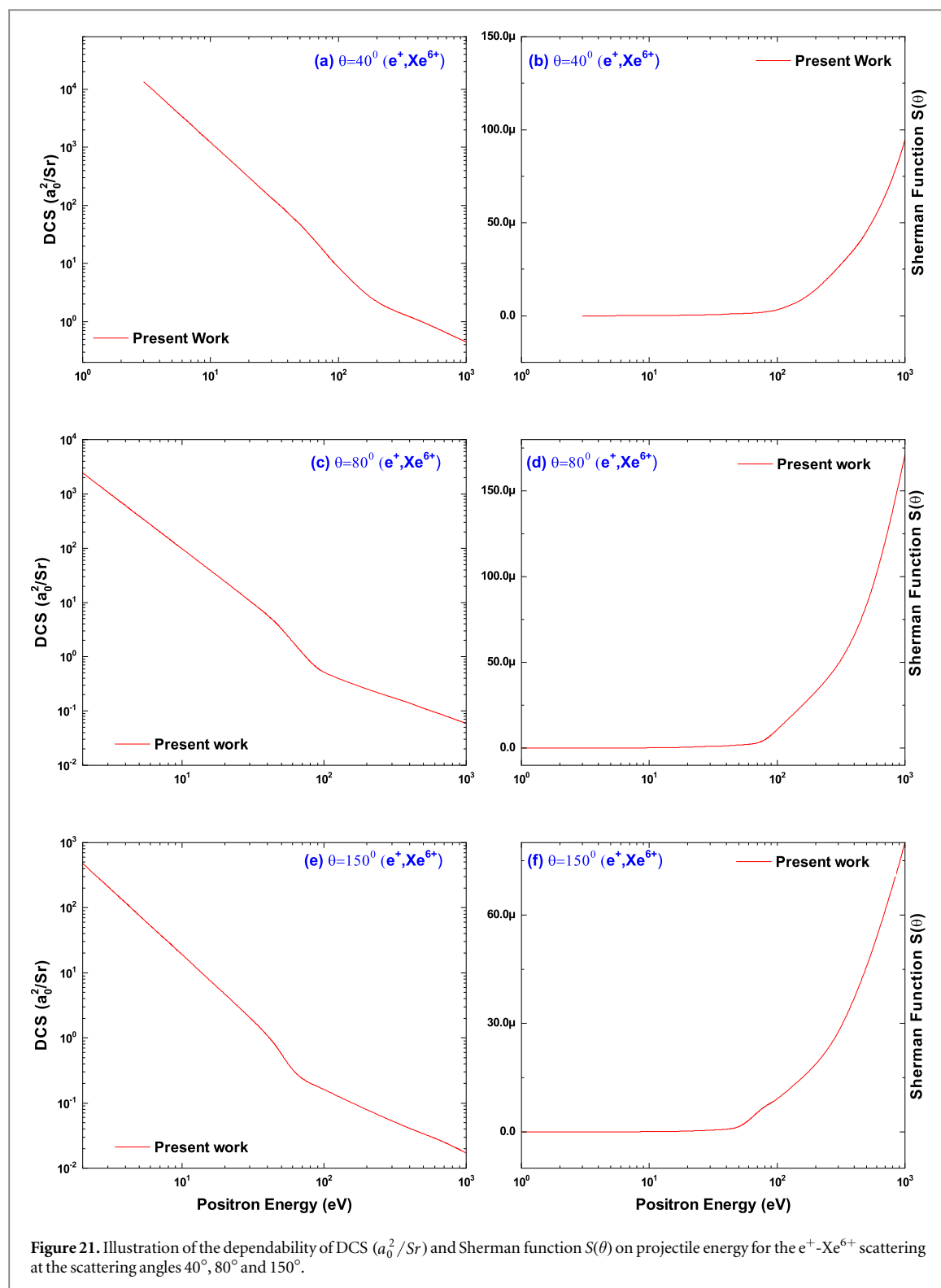


structure in DCS and Pronounced Coulomb glory. Low incident energy is enough to cause waning of interference structure from the angular distribution of elastically scattered electrons from ions of higher degree of ionicity and comparatively high incident energy causes this effect for ions of low ionicity. This matching of incident energy and degree of ionicity is pivotal for getting pronounced Coulomb glory.

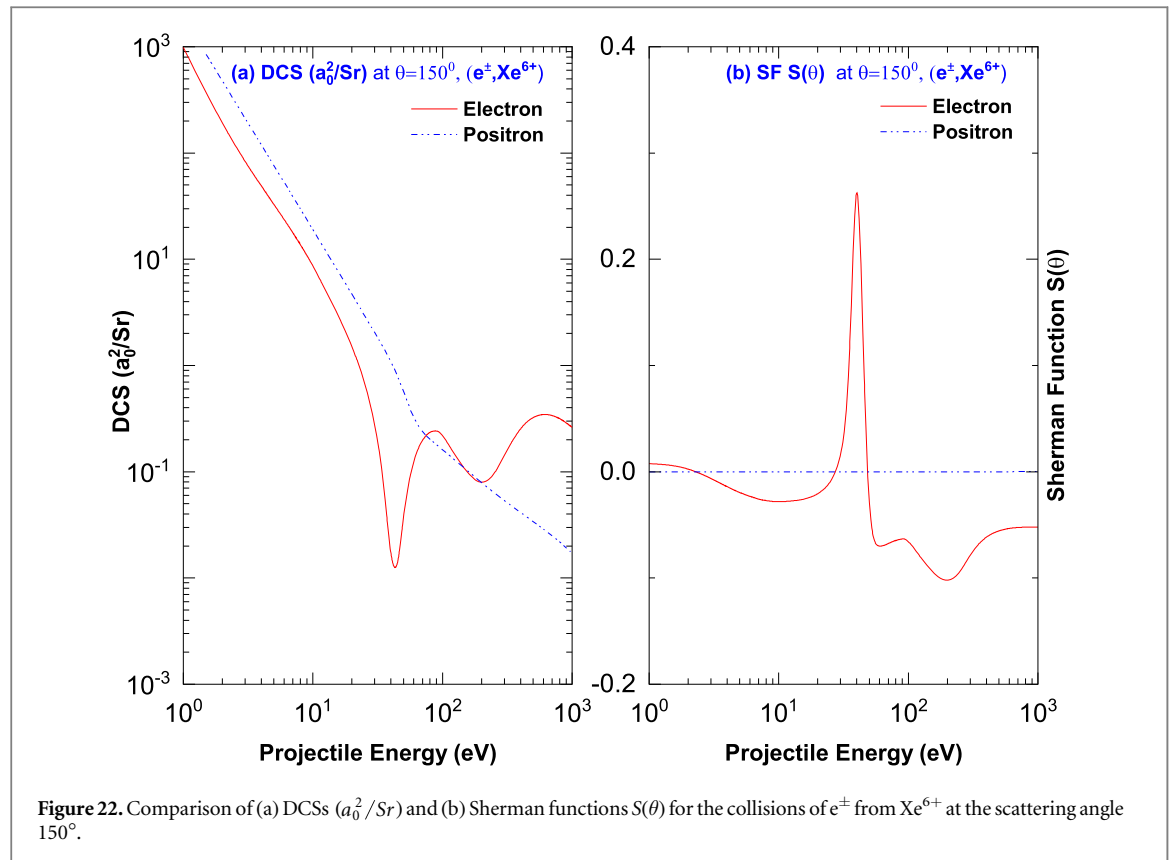
In figure 19, we present DCS at energies 20, 50 and 100 eV for the elastic scattering of positron from Xe^{q+} ($q = 1, 2, 10, 20, 25$ and 30). Rutherford like behavior is observed in positron scattering due to the repulsive central field which makes close encounters less probable. At high energy this behavior is also observed in electron scattering. There is no exchange scattering for positron scattering and at high energies contribution of exchange, polarization is negligible for electron scattering and hence we see this similarity.



In figure 20, we present the energy dependence of the DCS and of the corresponding Sherman function at 40° , 80° and 150° for electron scattering. The first one represents the scattering corresponding to large orbital angular momentum L causing lower angle of scattering. This scattering involving larger value of L reflects the Coulomb domination in the forward scattering resulting in the structureless DCS and very small value of Sherman function. The latter two angles are chosen to illustrate scattering at large and backward angles. Structures are observed for this lower values of impact parameter, responsible for these large-angle scattering that reveals the core penetration of the projectile electron into the target ion. Structures in DCS is observed to have relation with the structures in Sherman function in a manner that minima in the DCS correspond to maxima in $|S|$ approximately. In figure 21, we present the same as in figure 20 for positron scattering. As explained earlier, nearly monotonic pattern in DCS and low value of Sherman function is observed.



Comparisons between the energy dependent DCSs at 150° for the scattering of e^\pm from Xe^{6+} are presented in figure 22(a). Scattering for small impact parameter is manifested in the DCS of electron scattering through the observed structures. Rearrangement collisions contribute to the enhancement of DCS for electron scattering. But in case of positron scattering no such structure is observed. The reason behind this is that for this projectile, scattering with large impact parameter, a manifestation of Rutherford behavior, is more probable than that with small impact parameter. In figure 22(b), spin polarizations are compared for the same as in 22(a). A maximum at ~ 40 eV is observed corresponding to the minimum in DCS at ~ 40 eV for electron scattering. Spin polarization for positron scattering is extremely low compared to the electron scattering.



4. Conclusion

In the present work, Dirac relativistic partial wave analysis is used to investigate the elastic scattering of e^\pm -ion for the xenon isonuclear series employing a modified Coulomb potential. This methodology provides fairly realistic description of the collision. We predict observable quantities like, DCS, IECS, MTCS and Sherman function, for the scattering of electron and DCS and Sherman function for the scattering of positron off the ions of xenon isonuclear series. We also present the Coulomb glory effect, an amplification of elastic backscattering due to the attractive screened Coulomb potential, for neon, argon and xenon isonuclear series. Our results show a reasonable agreement with the available experimental data [9–11] and other theoretical calculations [10, 11]. Our investigation brings out that the degree of ionicity and the incident energy do have bearing on the variation of cross sections along the isonuclear series. Short-range potential can make contribution to the formation of interference pattern. Airy interference structure, due to the scattering of low energy electron for ions of low and intermediate degree of ionicity, is observed in DCS. This Airy structure is a feature of elastic collisions from the target of high atomic number that can serve as a provider of strong short-range potential. This feature is not eye-catching for the targets of low and intermediate atomic number [3, 12, 19]. The airy structure declines slowly with the increase of ionicity through the decrease of number and magnitude of the interference extrema. The sharp structure at specific charge state also declines with the rise of incident energy owing to the destructive interference of greater number of angular momentum waves. An increase in DCS with the increase of ionicity is seen at a particular angle and energy. Monotonic pattern is observed in the energy dependence of IECSs and MTCSs. Up to Xe^{18+} , these cross sections increase with the increase of ionicity over the presented energy domain, but remain almost constant beyond this degree of ionicity. The former is due to dominance of the screening effect of bound electrons and the latter is due the dominance of nuclear potential and diminution of screening effect. Coulomb glory is observed in the angular distribution of elastically scattered electrons. Strongest effect is observed to shift towards lower degree of ionicity owing to the strength of the potential of electronic cloud to scatter electron through $\theta = 180^\circ$. Width of the maximum and the ratio of ion DCS to Rutherford DCS increases with the increase of energy. It is also observed that at a particular energy the width of the strongest maximum increases and the ratio of ion DCS to Rutherford DCS decreases with the decrease of atomic number. The matching of incident energy and degree of ionicity is responsible for pronounced Coulomb glory effect. Interference structures are observed in the DCS for electron scattering. On the other hand almost Rutherford behavior is observed in case of positron scattering because of the repulsive central field preventing the core penetration of positron. High energy DCS of electron scattering resembles the DCS of positron

scattering due to the negligible high energy contribution of exchange and correlation-polarization potentials. For the refinement of the collision theory and electron-ion interaction, more experimental measurements and calculations of data are required.

Acknowledgments

Mahmudul H Khandker and M Masum Billah gratefully acknowledge the partial funding of University of Rajshahi through the project no-5/52/RU/Science-2/18-19.

ORCID iDs

Mahmudul H Khandker  <https://orcid.org/0000-0001-9097-923X>

M Masum Billah  <https://orcid.org/0000-0001-6987-0977>

Hiroshi Watabe  <https://orcid.org/0000-0001-6257-7735>

A K F Haque  <https://orcid.org/0000-0002-1735-3967>

M Alfaz Uddin  <https://orcid.org/0000-0003-3911-0074>

References

- [1] Müller A 1996 Fundamentals of electron-ion interaction *Hyperfine Interact.* **99** 31–45
- [2] Khandker M H, Haque A K F, Maaza M and Uddin M A 2019 Elastic scattering of electrons from the ions of argon isonuclear series *Phys. Scr.* **94** 075402
- [3] Shorifuddoza M, Khandker M H, Haque A K F, Watabe H and Uddin M A 2020 Theoretical investigation of the elastic scattering of by the ions of nitrogen isonuclear series *Phys. Scr.* **95** 085403
- [4] Brotton S J, McKenna P, Gribakin G and Williams I D 2002 Angular distribution for the elastic scattering of electrons from $\text{Ar}^{+}(3s^2 3p^5 2p)$ above the first inelastic threshold *Phys. Rev. A* **66** 062706
- [5] Jean P, Gillard W, Marcowith A and Ferrière K 2009 Positron transport in the interstellar medium *Astronomy & Astrophysics* **508** 1099–116
- [6] Delfino M 2004 Radioactive medical implant and method of manufacturing *US Patent* 6, 676 595
- [7] Rawlin V 1988 Internal erosion rates of a 10-kw xenon ion thruster XXIV *Joint Propulsion Conf.* p 2912
- [8] Doerner R P, Whyte D G and Goebel D M 2003 Sputtering yield measurements during low energy xenon plasma bombardment *J. Appl. Phys.* **93** 5816–23
- [9] McKenna P and Williams I D 2001 Differential cross section measurements for elastic scattering of electrons from Ar^{2+} and Xe^{2+} *Phys. Scr.* **2001** 370
- [10] Bélenger C, Defrance P, Friedlein R, Guet C, Jalabert D, Maurel M, Ristori C, Rocco J C and Huber B A 1996 Elastic large-angle scattering of electrons by multiply charged ions *J. Phys. B: At. Mol. Opt. Phys.* **29** 4443
- [11] Huber B A, Ristori C, Guet C, Küchler D and Johnson W R 1994 Elastic scattering of electrons from heavy multiply charged ions (Xe^{6+} , Xe^{8+} , and Ba^{2+}) *Phys. Rev. Lett.* **73** 2301
- [12] Khandker M H, Haque A K F, Maaza M and Alfaz Uddin M 2020 Scattering of e^{\pm} from the neon isonuclear series over the energy range 1 eV–0.5 GeV *Japan. J. Appl. Phys.* **59** SHHA05
- [13] Zouros T J M, Benis E P, Gorczyca T W, González A D, Zamkov M and Richard P 2003 Differential electron scattering from positive ions measured by zero-degree ion-atom spectroscopy *Nucl. Instrum. Methods Phys. Res., Sect. B* **205** 508–16
- [14] Demkov Y N 1993 Glory effect for the backscattering of negatively charged particles by multicharged ions *AIP Conf. Proc.* vol 274 (Manhattan, Kansas (USA): American Institute of Physics) pp 512–4
- [15] Demkov Y N, Ostrovskii V N and Tel'nov D A 1984 New type of cross section singularity in backward scattering: the coulomb glory *Zh. Eksp. Teor. Fiz.* **86** 450
- [16] Demkov Y N and Ostrovsky V N 2001 Enhanced backscattering in antiproton-atom collision: coulomb glory *J. Phys. B: At. Mol. Opt. Phys.* **34** L595
- [17] Maiorova A V, Tel'nov D A, Shabaev V M, Zaytsev V A, Plunien G and Stöhlker T 2010 The coulomb glory effect in collisions of antiprotons with heavy nuclei: relativistic theory *J. Phys. B: At. Mol. Opt. Phys.* **43** 205006
- [18] McEachran R P and Stauffer A D 2009 Calculation of elastic scattering of electrons from argon using an optical potential *Journal of Physics: Conf. Series* vol 194 (Bristol: IOP Publishing) p 042014
- [19] Khandker M H, Arony N T, Haque A K F, Maaza M, Masum Billah M and Uddin M A 2019 Scattering of e^{\pm} from N_2 in the energy range 1 eV–10 keV *Mol. Phys.* **118** 1–15
- [20] Williams I D 1999 Electron-ion scattering *Rep. Prog. Phys.* **62** 1431
- [21] Desclaux J P 1975 A multiconfiguration relativistic DIRAC-FOCK program *Comput. Phys. Commun.* **9** 31–45
- [22] Hahn B, Ravenhall D G and Hofstadter R 1956 High-energy electron scattering and the charge distributions of selected nuclei *Phys. Rev.* **101** 1131
- [23] Furness J B and McCarthy I E 1973 Semiphenomenological optical model for electron scattering on atoms *J. Phys. B: At. Mol. Phys.* **6** 2280
- [24] Perdew J P and Zunger A 1981 Self-interaction correction to density-functional approximations for many-electron systems *Phys. Rev. B* **23** 5048
- [25] Salvat F, Jablonski A and Powell C J 2005 Elsepa—dirac partial-wave calculation of elastic scattering of electrons and positrons by atoms, positive ions and molecules *Comput. Phys. Commun.* **165** 157–90
- [26] Jakubassa-Amundsen D H and Barday R 2012 The sherman function in highly relativistic elastic electron-atom scattering *J. Phys. G: Nucl. Part. Phys.* **39** 025102
- [27] Lide D R 1995 *CRC Handbook of Chemistry and Physics: A Ready-Reference Book of Chemical and Physical Data* (Boca Raton, FL: CRC Press)
- [28] Mittleman M H and Watson K M 1960 Effects of the pauli principle on the scattering of high-energy electrons by atoms *Ann. Phys.* **10** 268–79
- [29] Salvat F 2003 Optical-model potential for electron and positron elastic scattering by atoms *Phys. Rev. A* **68** 012708

- [30] Jain A 1990 Low-energy positron-argon collisions by using parameter-free positron correlation polarization potentials *Phys. Rev. A* **41** 2437
- [31] Rose M E 1961 *Relativistic Electron Theory* (New York: Wiley)
- [32] Kessler J 1969 Electron spin polarization by low-energy scattering from unpolarized targets *Rev. Mod. Phys.* **41** 3
- [33] Maiorova A V, Telnov D A, Shabaev V M, Tupitsyn I I, Plunien G and Stöhlker T 2007 Backward scattering of low-energy antiprotons by highly charged and neutral uranium: coulomb glory *Phys. Rev. A* **76** 032709
- [34] Srigengan B, McKenna P, McGuinness P and Williams I D 1999 Elastic scattering of electrons from argon ions *Phys. Scr.* **1999** 272